Running Title: DNA repair dysfunction and PARPi in lobular breast cancer

Research article

Co-regulator activity of Mediator of DNA Damage Checkpoint 1 (MDC1) is associated with DNA repair dysfunction and PARP inhibitor sensitivity in lobular carcinoma of the breast

Joseph L. Sottnik[1], Madeleine T. Shackleford[1], Amanda L. Richer[2,3], Rui Fu[2,3], Jay R. Hesselberth[2,3], Matthew J. Sikora[1,3]

Affiliations

[1]Dept. of Pathology, University of Colorado Anschutz Medical Campus

[2]Dept. of Biochemistry and Molecular Genetics, University of Colorado Anschutz Medical Campus

[3]RNA Bioscience Initiative, University of Colorado School of Medicine

Corresponding author

Matthew J. Sikora, PhD.; Mail Stop 8104, Research Complex 1 South, Room 5110, 12801 E. 17th Ave.; Aurora, CO 80045. Tel: (303)724-4301; Fax: (303)724-3712; email: matthew.sikora@cuanschutz.edu. Twitter: @mjsikora

Authors' contributions

MJS conceived of the project and experiments. JLS, MTS, and ALR designed and performed experiments. JLS developed models for the project. All authors contributed to data analysis and interpretation. MJS wrote the draft manuscript; all authors read and revised the manuscript and have read and approved of this version of the manuscript.

Funding

This work was supported by ACS RSG-20-042-01-DMC from the American Cancer Society (MJS), by R01 CA251621 from the National Institutes of Health (MJS), by grants from the Cancer League of Colorado, Inc (MJS), by support from the Dynami Foundation (MJS), by the Lobular Breast Cancer Research Fund at CU Anschutz (MJS), and by a grant from the RNA Bioscience Initiative at the CU Anschutz School of Medicine (MJS). This work utilized the U. Colorado Cancer Center Genomics Shared Resource, Biostatistics and Bioinformatics Shared Resource, Cell Technologies Shared Resource (RRID: SCR_021982), and Flow Cytometry Shared Resource (RRID: SCR_022035) supported by P30 CA046934. The content of this

manuscript is solely the responsibility of the authors and does not necessarily represent the official views of the National Institutes of Health or other agencies.

Key words
Invasive lobular carcinoma, breast cancer, MDC1, estrogen receptor, DNA repair, DNA damage response, PARP inhibitors.

ABSTRACT

Invasive lobular carcinoma of the breast (ILC) are typically estrogen receptor α (ER)-positive and present with biomarkers of anti-estrogen sensitive disease, but growing laboratory and clinical data, including poor long-term outcomes faced by patients with ILC, suggest endocrine response and ER function are unique in ILC. We previously identified the DNA repair protein Mediator of DNA Damage Checkpoint 1 (MDC1) as an ILC-specific ER co-regulator necessary for ER genomic activity, and that MDC1 co-regulator activity was associated with dysfunctional canonical DNA repair roles of MDC1. To understand these potentially reciprocal activities of MDC1 in ILC, we profiled the MDC1 interactome and found that MDC1 associated proteins in ILC cells mirror a "BRCA-mutant" state lacking MDC1 interaction with key homologous recombination (HR) proteins. Single-cell gene expression and DNA repair activity showed that specific activation of ER:MDC1 target genes was associated with increased PARP-associated DNA repair and decreased HR gene expression. These data suggest that HR is dysfunctional in ILC, which was supported by a lack of DNA damage-induced RAD51 turnover in ILC cells, and an elevated DNA damage response protein signature in a subset of ILC tumors. We tested whether this HR dysfunction could be exploited using PARP inhibition, and found that talazoparib treatment produced a durable growth suppression both *in vitro* and in ILC cell line xenografts *in vivo*. The ILC-specific ER:MDC1 association creates a new context for ER and MDC1 function in ILC, at the cost of a DNA repair dysfunction that may be therapeutically targetable.

Significance: ILC are rarely associated with biomarkers of overt HR deficiency, as such patients are rarely eligible for treatment with PARP inhibitors. Our work suggests ILC present with a previously unappreciated form of HR dysfunction, linked to ILC-specific genomic activity of ER, that imparts sensitivity to PARP inhibition.

INTRODUCTION

Invasive lobular carcinoma of the breast (ILC) is increasingly recognized as a distinct clinical and molecular entity among breast cancers (1–3). Beyond ILC's unique histopathological presentation – i.e., infiltrating the breast in a discohesive, "single-file" pattern – we now appreciate that ILC have distinct genetic and cellular features relative to breast cancers of no special type (also known as invasive ductal carcinoma, IDC). Most ILC present with biomarkers of low-risk disease, as ~95% are estrogen receptor α (ER)-positive and ~80% are classified in the Luminal A molecular subtype (4), but retrospective studies suggest that ILC carry more long-term risk of poor outcomes than IDC. Retrospective studies have shown that 5-8 years after diagnosis, ILC recurrences increase relative to IDC regardless of ER status (5–7). Further, recurrent or metastatic ILC presents distinct challenges, as ILC are unique among breast cancers in metastasizing to the GI/GU, peritoneum, ovary/uterus, and the orbit (2,5,8). Treating ILC is further complicated due to controversies related to anti-estrogen resistance (9), the limited benefit of chemotherapy for most patients with ILC (2,10,11), and the lack of any available precision or targeted treatments designed for ILC. New treatments for patients with ILC are needed, but strategies must be driven by advances in defining the unique biology of ILC.

We previously profiled the ER interactome in ILC cells with the goal of defining novel ER co-regulators that mediate ILC-specific endocrine response or anti-estrogen resistance (12). This approach identified Mediator of DNA Damage Checkpoint 1 (MDC1) as a critical ER co-regulator specifically in ILC cells. We found that the ER:MDC1 interaction is likely unique to ILC cells, MDC1 was specifically required for ER-driven growth in ILC but not IDC cells, and MDC1 knockdown broadly dysregulated the ER transcriptome in ILC cells. As MDC1 has no known enzymatic activity, the mechanism by which MDC1 co-regulates ER is unknown. The canonical role of MDC1, however, is to bind new phospho-H2AX (γH2AX) marks at DNA double-strand breaks and scaffold double-strand break repair machinery, including the MRE11/RAD50/NBS1 (MRN) complex and additional downstream partners that ultimately facilitate repair (13–15). The MDC1 scaffold initiates signaling via CHK1/2 to cause cell cycle arrest, and coordinates DNA double-strand break repair either via homologous recombination (HR) or non-homologous end joining (NHEJ). While we confirmed these canonical DNA repair roles of MDC1 in IDC cells, this was not the case in ILC cells. For example, γH2AX foci formation, which requires MDC1 (16), was limited in ILC cells and γH2AX instead presented as an elevated pan-nuclear signal; pan-nuclear γH2AX has been linked to DNA repair dysfunction (17). These observations collectively suggest that the novel ER co-regulator activity of MDC1 may come at a cost of compromised MDC1 activity in DNA repair.

ILC do not typically present with biomarkers of overt DNA repair deficiency such as germline *BRCA1/2* mutations. These mutations are uncommon in ILC and are depleted relative to IDC; ILC accounts for up to 15% of all breast cancers, but only ~2% and ~8% of breast cancers in *BRCA1* or *BRCA2* mutation carriers, respectively, and germline *TP53* mutations are also rare in ILC (18–20). Similarly, somatic mutations in genes

associated with DNA repair are uncommon in primary ILC, e.g. somatic *TP53* mutations were found in only ~8% of ILC, and only 5.7% of Luminal A ILC, in the Cancer Genome Atlas (TCGA)(4). ILC genomes are typically considered 'quiet' and overall show fewer structural re-arrangements than other breast cancers, though indels are detected at similar rates. Similarly, HR deficiency as defined by various mutational signatures is not common in ILC but is typically associated with the few ILC that are *TP53*-mutant or with germline *BRCA1/2* mutations (3). Together these observations would suggest that DNA repair deficiency is uncommon in ILC. However, data from TCGA show that a putative transcriptional subtype of ILC, "Proliferative" ILC, was associated with an elevated DNA damage response signature in protein array analyses (discussed further below) (4). This is paralleled by the identification of frequent *MDM4* amplification in ILC tumors (17%) (21). MDM4 was required for proliferation and survival of *TP53*-wild type ILC cell lines, as such, suppression of p53-driven pathways by mechanisms independent of *TP53* mutation may be an underappreciated feature of ILC. Collectively these data suggest that our understanding of DNA repair signaling and function in ILC is incomplete, and may not be adequately defined as 'proficient' versus 'deficient', as it relates to *BRCA1/2* mutant tumors.

Based on the novel ER:MDC1 interaction in ILC cells and putative link to DNA repair dysfunction, we hypothesized that profiling the MDC1 interactome in ILC cells would both shed light on mechanisms by which MDC1 acts as an ER co-regulator, and offer insight into DNA repair function in ILC cells. These studies confirmed connections between the co-regulator activity versus DNA repair functions of MDC1, and identified potential mechanistic underpinnings of a "BRCA-like" phenotype in ILC cells. We explored whether MDC1-related "molecular BRCAness" in ILC cells provided opportunities for synthetic lethal therapeutic approaches. Better understanding of the cross-talk linking ER:MDC1, transcriptional regulation, and DNA repair capacity offers unique opportunities to understand ILC biology and develop precision treatments around synthetic vulnerabilities unique to ILC.

RESULTS

The MDC1 interactome in ILC cells indicates DDR dysfunction but active epigenomic functions

We profiled the MDC1 interactome in ILC cells to identify transcriptional co-regulator partners of ER:MDC1, and to assess differential MDC1 association with canonical DNA repair partners, by performing MDC1 co-immunoprecipitation + mass spectrometry (IP/MS) in ILC versus IDC cells. Of note, proteomic approaches have previously shown MDC1 association with the MRN complex and other DNA repair proteins, but studies to date have used exogenous and/or tagged versions of full-length MDC1 or MDC1 fragments, and have only been performed in HeLa, HEK293 (293), or U2OS cells (22–26). We performed endogenous MDC1 IP using a validated MDC1 antibody (see Methods) from ER+ cell lines MCF7 (IDC), HCC1428 (IDC, *BRCA2*-

mutant), MM134 (ILC), and 44PE (ILC), as well as 293FT cells (to compare our approach to literature data). IP/MS was performed absent DNA damaging agents, from biological duplicate MDC1 IP samples and a matched IgG control per cell line; an additional series of samples for MM134 was treated with the anti-estrogen fulvestrant for 24hrs prior to IP. MS parameters and analyses are described in Material and Methods. MDC1 was strongly enriched in targeted IP versus IgG across all samples (MDC1 iBAQ: ~90-fold up to >1000-fold for MDC1 IP vs IgG, **Supplemental Figure 1A**).

Across all 5 cell lines, over 2000 proteins were enriched relative to IgG controls (**Supplemental File 1**). Identified proteins were most enriched for ribosomal and related mRNA/rRNA-processing proteins (as observed by Salifou et al, discussed below (24)).We excluded/filtered RNA processing proteins to facilitate further analysis (see Methods), yielding n=1666 proteins identified in at least one cell line (**Supplemental File 1**). We first examined MDC1-associated proteins in 293FT cells (n=1497, n=1236 after filtering), and confirmed that the MRN complex (MRE11, RAD50, NBN), constitutive partners of MDC1 in 293FT and other cells, were strongly enriched (**Supplemental Figure 1B**). More broadly, DNA repair pathway proteins were strongly enriched as well as epigenomic proteins, consistent with the functions of epigenomic proteins in DNA repair and reported roles for MDC1 in chromatin remodeling (27) (**Supplemental Figure 1C, Supplemental File 1**).

We compared our 293FT data to MDC1 interactome data from Salifou et al (24), the only other proteome-wide MDC1 interactome data published to date. Whereas we utilized an MDC1-specific antibody for IP, Salifou et al used CRISPR/Cas9 to append a Flag-hemagglutinin (HA) tag to the N-terminus of endogenous MDC1 in 293FT cells, then performed tandem affinity purification of Flag/HA-MDC1, reporting n=384 MDC1 associated proteins (n=276 after filtering as above). As noted above, both datasets were strongly enriched for splicing and translational proteins (**Supplemental Figure 2A**), supporting a role for MDC1 in protecting genomic integrity at actively transcribed sites (24,28). Upon filtering, our data using direct MDC1 IP was specifically enriched in DNA repair and chromatin remodeling proteins (**Supplemental Figure 2B**). Of note, our data included greater depth of coverage of similar biological pathways compared to the Flag/HA-MDC1 dataset (**Supplemental Figure 2C**), and proteins in pathways enriched only in the Flag/HA-MDC1 dataset were still identified in our data (**Supplemental Figure 2D**). These data support that our direct MDC1 IP with MS confirmed prior observations on MDC1 association with mRNA/translational machinery yet provided greater representation and enrichment for MDC1-associated DNA repair and chromatin remodeling proteins.

In the breast cancer cell lines >700 MDC1-associated proteins were identified in all lines after filtering (**Figure 1A**). Hierarchical clustering showed that the MDC1 interactome in ILC cells was distinct from MCF7 (IDC) cells and more closely related to the *BRCA2*-mutant HCC1428 cells (**Figure 1A**), which was consistent with a relative depletion of MDC1-associated DNA repair proteins. DNA repair proteins were enriched overall in all 4 lines (**Supplemental File 1**); however, though NHEJ and nucleotide-excision repair were enriched in

ILC cells, HR proteins were enriched only in MCF7 but depleted in the ILC and *BRCA2*-mutant cells (**Figure 1B**). This depletion of HR proteins included minimal/absent MRN complex proteins and other HR factors (**Figure 1C**). Conversely, despite the depletion of DDR/HR proteins, the MDC1 interactome in ILC cells was strongly enriched for epigenomic partners (**Figure 1D**), notably including histone acetylation proteins. Distinct subsets of histone acetylation factors were identified in MCF7/IDC vs ILC (and *BRCA2*-mutant) cells, e.g. RUVBL1/2 in the former and the HBO1-complex (ING5, BRPF3, MEAF6, JADE3) in the latter (**Figure 1E**). Collectively these data suggest that the constitutive association of MRN with MDC1 may not be absolute, and that the absence/depletion of MRN on MDC1 is associated with DNA repair/HR dysfunction. The depletion of MRN and other HR proteins among MDC1-associated proteins in ILC is consistent with the pan-nuclear gH2AX localization we previously reported (12). However, the epigenomic functions of MDC1 likely remain intact despite DDR dysfunction and thus may be associated with the co-regulator functions of MDC1 in ILC cells.

Inhibiting estrogen receptor in ILC cells restores DDR/HR proteins in the MDC1 interactome

We hypothesized that the novel ER:MDC1 interaction in ILC cells is at least in part responsible for remodeling the MDC1 interactome, and tested this by treating MM134 cells with the ER antagonist and degrader fulvestrant prior to MDC1 IP/MS. Hierarchical clustering showed that with fulvestrant the MDC1 interactome in MM134 more closely resembled MCF7 cells (i.e. HR-competent cells; **Figure 2A**). Strikingly, this change was associated with increased MDC1-association with HR pathway proteins (**Figure 2B**), including the MRN complex, specifically MRE11 and RAD50 (**Figure 2C**). Notably, HR proteins gained in MM134+Fulv versus MM134 (**Figure 2C**, orange bar) were all identified as MDC1-associated in MCF7 cells, suggesting that these MDC1 interactions were restored with fulvestrant treatment, rather than fulvestrant driving new MDC1 interactions. MDC1 association with epigenomic proteins remained enriched in fulvestrant treated cells (**Figure 2D**), but we noted changes in the specific proteins identified. In particular, among histone acetylation proteins, several proteins were shifted by fulvestrant treatment to resemble the state in MCF7 cells, including restoration of RUVBL2 and depletion of HBO1-complex proteins ING5, JADE3, and BRPF3 (**Figure 2E**, orange bar). These observations support that ER plays a role in regulating the genomic functions of MDC1 at least in part through control over the MDC1 interactome.

Co-regulator activity of MDC1 is linked to specific cellular DNA repair activity

We explored the cross-talk between MDC1 co-regulator activity with ER versus MDC1 DNA repair activity with a single-cell approach to measure DNA repair called “Haircut”. Haircut profiles DNA repair

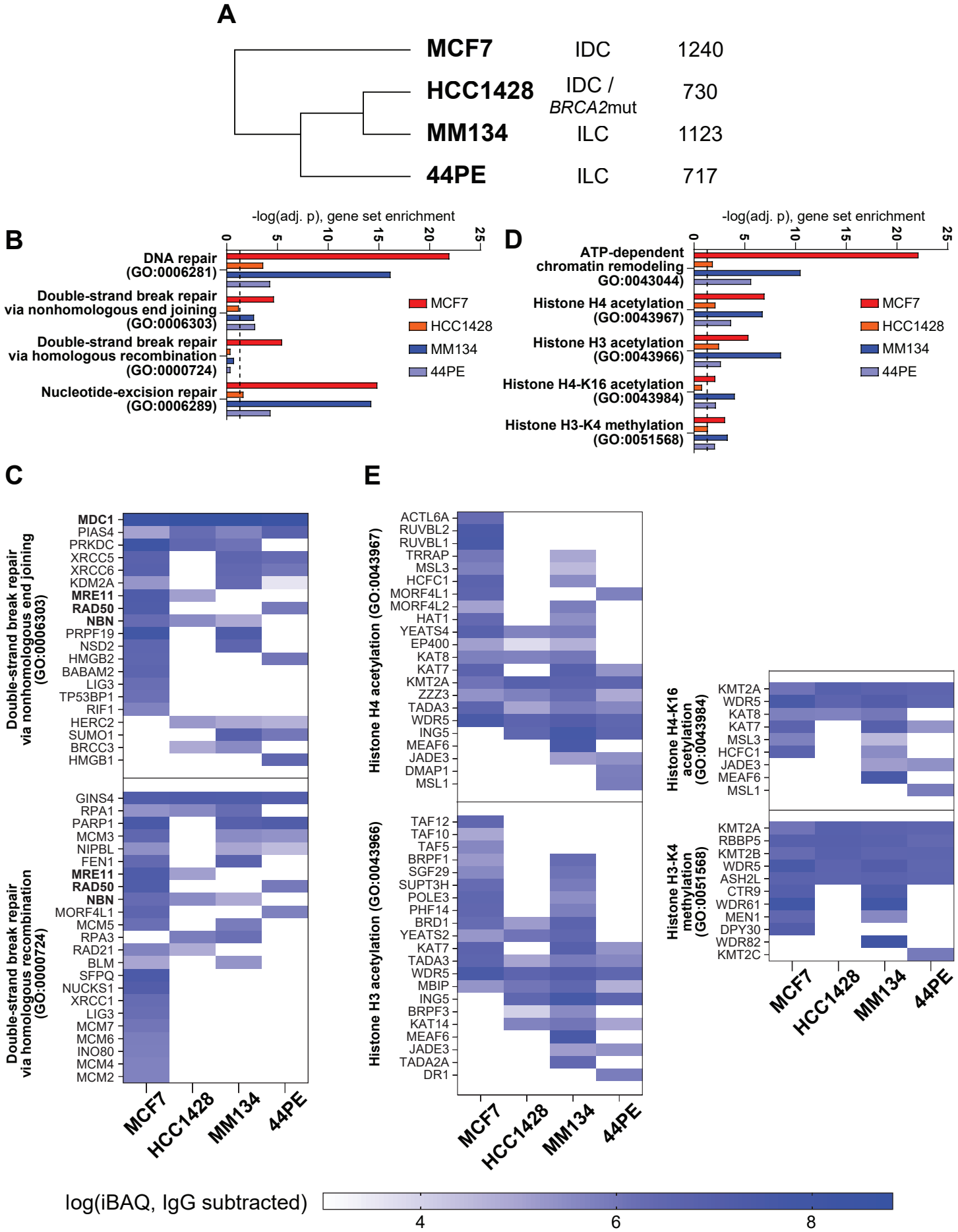
A
MCF7
IDC
1240
HCC1428
IDC / BRCA2mut
730
MM134
ILC
1123
44PE
ILC
717
B
-log(adj. p), gene set enrichment
0
5
10
15
20
25
DNA repair (GO:0006281)
Double-strand break repair via nonhomologous end joining (GO:0006303)
Double-strand break repair via homologous recombination (GO:0000724)
Nucleotide-excision repair (GO:0006289)
MCF7
HCC1428
MM134
44PE
D
-log(adj. p), gene set enrichment
ATP-dependent chromatin remodeling GO:0043044)
Histone H4 acetylation (GO:0043967)
Histone H3 acetylation (GO:0043966)
Histone H4-K16 acetylation (GO:0043984)
Histone H3-K4 methylation (GO:0051568)
MCF7
HCC1428
MM134
44PE
C
Double-strand break repair via nonhomologous end joining (GO:0006303)
MDC1
PIAS4
PRKDC
XRCC5
XRCC6
KDM2A
MRE11
RAD50
NBN
PRPF19
NSD2
HMGB2
BABAM2
LIG3
TP53BP1
RIF1
HERC2
SUMO1
BRCC3
HMGB1
Double-strand break repair via homologous recombination (GO:0000724)
GINS4
RPA1
PARP1
MCM3
NIPBL
FEN1
MRE11
RAD50
NBN
MORF4L1
MCM5
RPA3
RAD21
BLM
SFPQ
NUCKS1
XRCC1
LIG3
MCM7
MCM6
INO80
MCM4
MCM2
MCF7
HCC1428
MM134
44PE
E
Histone H4 acetylation (GO:0043967)
ACTL6A
RUVBL2
RUVBL1
TRRAP
MSL3
HCFC1
MORF4L1
MORF4L2
HAT1
YEATS4
EP400
KAT8
KAT7
KMT2A
ZZZ3
TADA3
WDR5
ING5
MEAF6
JADE3
DMAP1
MSL1
Histone H3 acetylation (GO:0043966)
TAF12
TAF10
TAF5
BRPF1
SGF29
SUPT3H
POLE3
PHF14
BRD1
YEATS2
KAT7
TADA3
WDR5
MBIP
ING5
BRPF3
KAT14
MEAF6
JADE3
TADA2A
DR1
MCF7
HCC1428
MM134
44PE
Histone H4-K16 acetylation (GO:0043984)
KMT2A
WDR5
KAT8
KAT7
MSL3
HCFC1
JADE3
MEAF6
MSL1
Histone H3-K4 methylation (GO:0051568)
KMT2A
RBBP5
KMT2B
WDR5
ASH2L
CTR9
WDR61
MEN1
DPY30
WDR82
KMT2C
MCF7
HCC1428
MM134
44PE
log(iBAQ, IgG subtracted)
4
6
8

Figure 1. MDC1 interactome in ILC cells mirrors a BRCA-mutant state. (A) Hierarchical clustering (Pearson) of MDC1 associated proteins after filtering of RNA-processing related proteins. **(B,D)** Gene set enrichment against GO Biological Processes. Dashed line: adj. p = 0.05. **(C,E)** Mean IgG-subtracted intensity of duplicate IP/MS samples for proteins in indicated ontology groups.

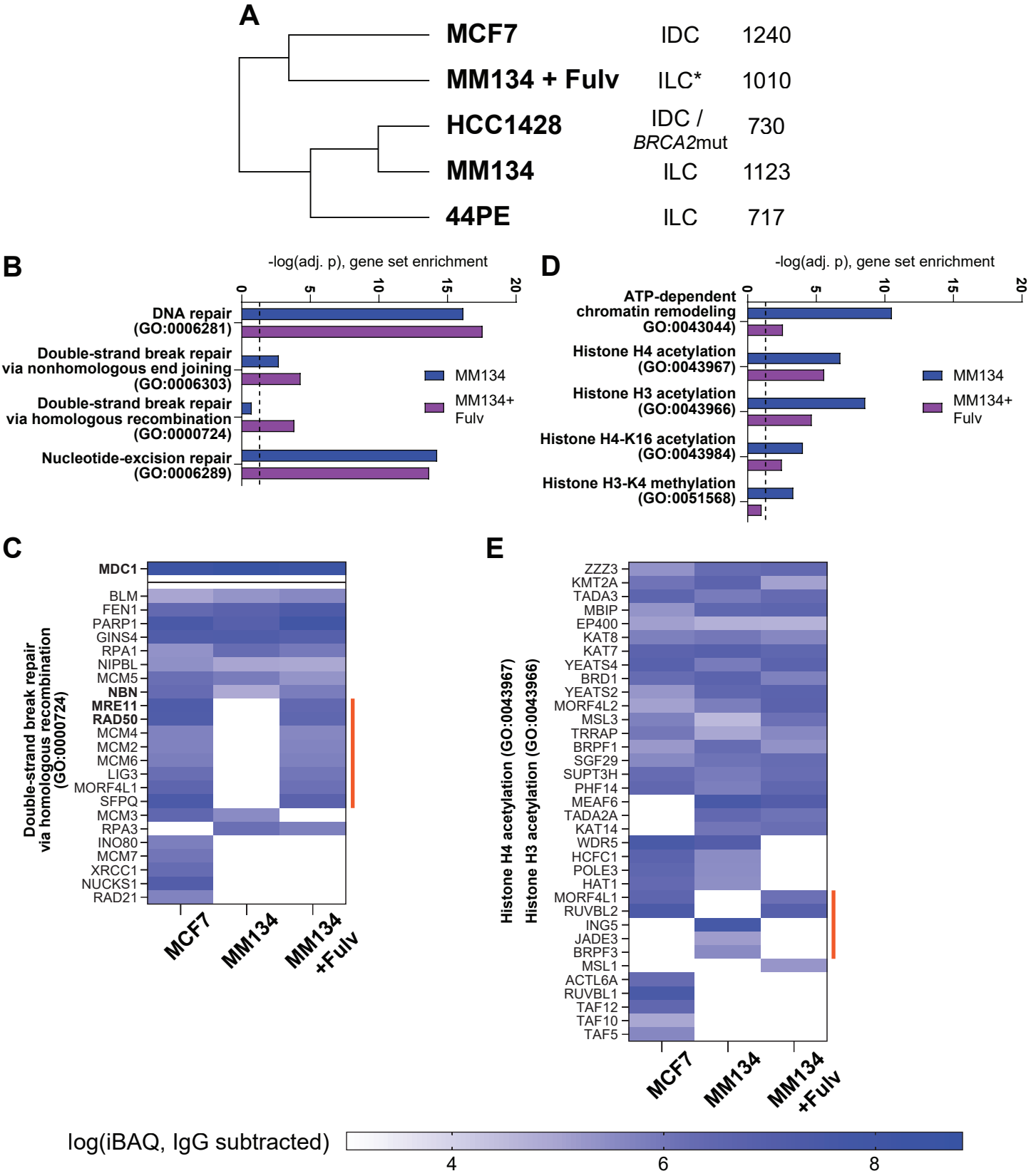
A
MCF7
IDC
1240
MM134 + Fulv
ILC*
1010
HCC1428
IDC / BRCA2mut
730
MM134
ILC
1123
44PE
ILC
717
B
-log(adj. p), gene set enrichment
0
5
10
15
20
DNA repair (GO:0006281)
Double-strand break repair via nonhomologous end joining (GO:0006303)
Double-strand break repair via homologous recombination (GO:0000724)
Nucleotide-excision repair (GO:0006289)
MM134
MM134+ Fulv
D
-log(adj. p), gene set enrichment
0
5
10
15
20
ATP-dependent chromatin remodeling GO:0043044)
Histone H4 acetylation (GO:0043967)
Histone H3 acetylation (GO:0043966)
Histone H4-K16 acetylation (GO:0043984)
Histone H3-K4 methylation (GO:0051568)
MM134
MM134+ Fulv
C
Double-strand break repair via homologous recombination (GO:0000724)
MDC1
BLM
FEN1
PARP1
GINS4
RPA1
NIPBL
MCM5
NBN
MRE11
RAD50
MCM4
MCM2
MCM6
LIG3
MORF4L1
SFPQ
MCM3
RPA3
INO80
MCM7
XRCC1
NUCKS1
RAD21
MCF7
MM134
MM134 +Fulv
E
Histone H4 acetylation (GO:0043967)
Histone H3 acetylation (GO:0043966)
ZZZ3
KMT2A
TADA3
MBIP
EP400
KAT8
KAT7
YEATS4
BRD1
YEATS2
MORF4L2
MSL3
TRRAP
BRPF1
SGF29
SUPT3H
PHF14
MEAF6
TADA2A
KAT14
WDR5
HCFC1
POLE3
HAT1
MORF4L1
RUVBL2
ING5
JADE3
BRPF3
MSL1
ACTL6A
RUVBL1
TAF12
TAF10
TAF5
MCF7
MM134
MM134 +Fulv
log(iBAQ, IgG subtracted)
4
6
8

Figure 2. ER inhibition with fulvestrant shifts MDC1 interactome toward a non-BCRA-mutant state. (A) Hierarchical clustering (Pearson) of MDC1 associated proteins as in Figure 1A, with inclusion of MM134+Fulvestrant samples. **(B,D)** Gene set enrichment against GO Biological Processes. Dashed line: adj. p = 0.05. **(C,E)** Mean IgG-subtracted intensity of duplicate IP/MS samples for proteins in indicated ontology groups. Orange bar identifies IP/MS hits putative remodeled by fulvestrant treatment discussed in text.

activities using DNA oligo substrates for specific repair enzymes by including oligonucleotide substrates in the single-cell emulsion. Repair enzymes create nicks in the substrates, and sequencing quantifies repair activities by comparing modified and unmodified oligo substrates. Haircut profiles PARP-related single-strand repair, quantifying the activity of base excision repair and nucleotide excision/incision repair enzymes in a single reaction (See Figures 1-2 and Supplemental Figure 1 in (29), also (30)). We coupled Haircut with targeted transcriptome analysis (10X Genomics Pan-cancer capture panel, n=1,253 genes), allowing us to profile DNA repair activity and gene expression in individual cells. We performed scRNAseq + Haircut in MM134 ±E2 (n=8,307 cells: –E2, n=4,940; +E2, n=3,367) (**Supplemental File 2** – see access link in methods). We extrapolated ER activity and co-regulator activity (MDC1 vs pioneer factor FOXA1; **Figure 3A**) from the expression of n=259 ER target genes in the capture panel based on our prior RNAseq study (12) (cell cycle genes excluded; **Supplemental File 2**), and examined ER:MDC1 activity versus DNA repair capacities.

Gene expression via the Pan-cancer capture panel defined 8 clusters (**Figure 3B**), which showed distinct ER and co-regulator activity (**Figure 3C**; **Supplemental Figure 3A**). Two clusters were primarily –E2 cells and showed minimal activation of ER target genes (Clusters 6 & 2), while the remaining clusters had increasing fractions of +E2 cells and had differential activation of ER target genes. In two clusters, ER:MDC1 target genes were active while MDC1-independent ER target genes were inactive (**Figure 3C**, clusters 5 & 7; C5/C7). Paralleling this separate activation of MDC1-dependent vs –independent ER target genes, we noted that activation of MDC1-dependent ER targets was overall independent of cell cycle status, whereas MDC1-independent ER targets showed an E2-independent activation in S and G2/M versus G1 (**Supplemental Figure 3B**). Importantly, the specific activation of ER:MDC1 in C5 and C7 and distinct cell cycle context supports that MDC1 has a distinct role in co-regulating ER relative to other factors like FOXA1, that is, ER:MDC1 gene regulation activity is separate from ER:FOXA1.

Notably, C5/7 largely lacked S-phase cells and were enriched for G1 and G2/M cells (as defined by gene expression), respectively. Despite the enrichment for G2/M cells in C7, both C5/7 expressed markedly low levels of genes associated with HR (**Figure 3D**), similar to the predominantly –E2/G1 phase clusters 6 & 2. C5/7 were similarly distinct in DNA repair capacity in Haircut analysis. The Haircut "Abasic" reporters primarily measure base excision repair (BER) activity of the enzyme APE1, and we found that +E2 cells had lower BER/APE1 activity versus –E2 cells (**Figure 3E**). In contrast, C5/7 showed elevated BER/APE1 activity and had the highest such activity among the +E2 clusters (**Figure 3F**). The ER target gene activity and Haircut data taken together link MDC1 co-regulator activity is to distinct DNA repair activity, and a potential reliance on non-HR pathways to maintain genomic integrity. These observations parallel the putative HR dysfunction indicated by the MDC1 interactome in ILC cells.

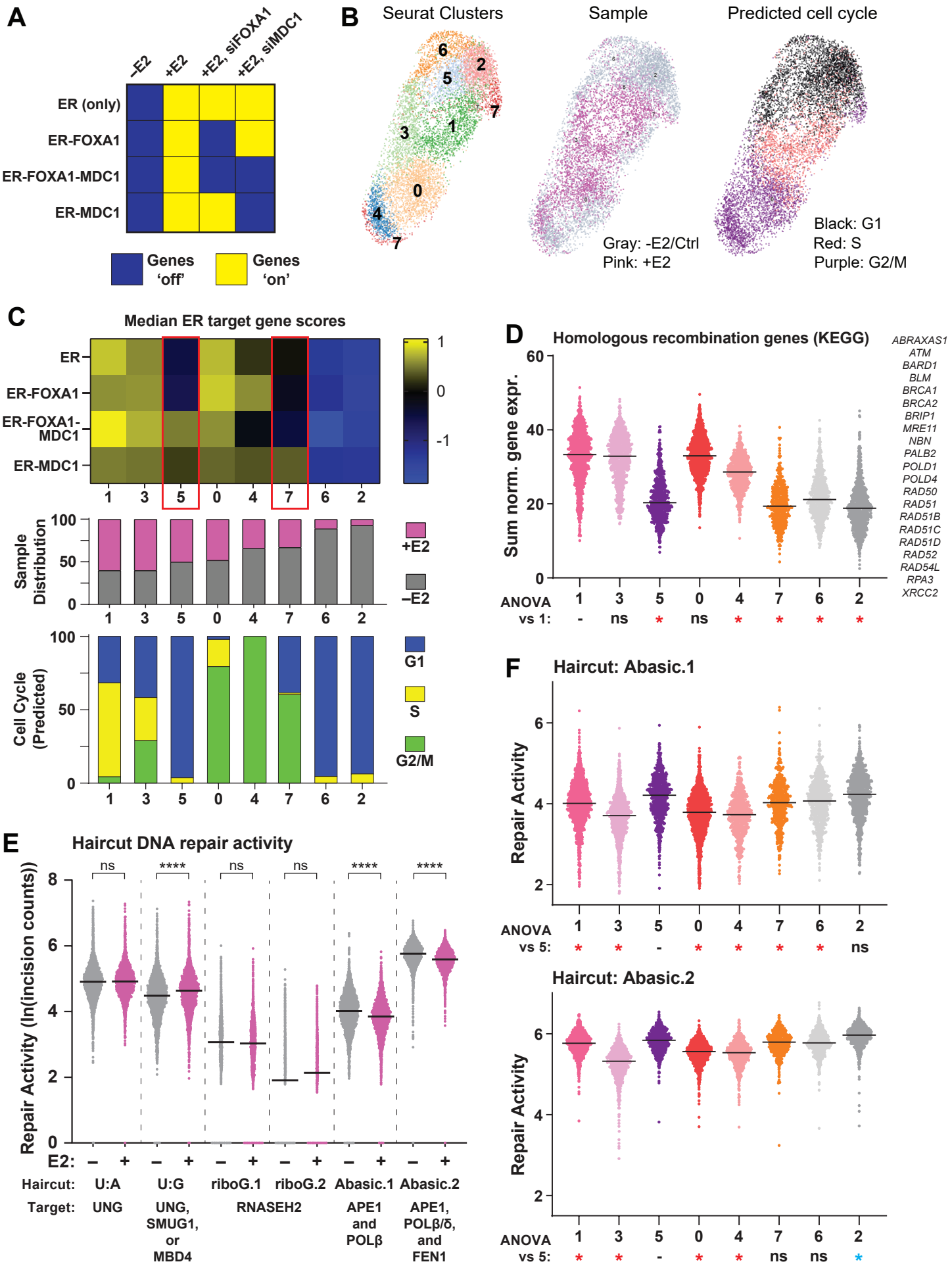
A
–E2
+E2
+E2, siFOXA1
+E2, siMDC1
ER (only)
ER-FOXA1
ER-FOXA1-MDC1
ER-MDC1
Genes 'off'
Genes 'on'
B
Seurat Clusters
Sample
Predicted cell cycle
Gray: -E2/Ctrl
Pink: +E2
Black: G1
Red: S
Purple: G2/M
C
Median ER target gene scores
ER
ER-FOXA1
ER-FOXA1-MDC1
ER-MDC1
Sample Distribution
+E2
–E2
Cell Cycle (Predicted)
G1
S
G2/M
D
Homologous recombination genes (KEGG)
Sum norm. gene expr.
ABRAXAS1
ATM
BARD1
BLM
BRCA1
BRCA2
BRIP1
MRE11
NBN
PALB2
POLD1
POLD4
RAD50
RAD51
RAD51B
RAD51C
RAD51D
RAD52
RAD54L
RPA3
XRCC2
ANOVA vs 1:
E
Haircut DNA repair activity
Repair Activity (ln(incision counts))
E2:
Haircut: U:A U:G riboG.1 riboG.2 Abasic.1 Abasic.2
Target: UNG UNG, SMUG1, or MBD4 RNASEH2 APE1 and POLβ APE1, POLβ/δ, and FEN1
F
Haircut: Abasic.1
Repair Activity
ANOVA vs 5:
Haircut: Abasic.2

Figure 3. Single cell transcriptome + Haircut data identifies reciprocal MDC1 co-regulator activity versus DNA repair activity. (A) Schematic for predicted ER target gene expression based on dependence on MDC1, FOXA1, or neither factor. Based on RNAseq data from Sottnik & Bordeaux et al, 2021. **(B)** UMAP plot showing Seurat clusters (left), sample/treatment (center), and predicted cell cycle state (right). **(C)** Top, ER target gene scores in each of the 8 Seurat clusters. Single cell scores are a z-score of the relative expression of estrogen-induced and estrogen-repressed genes (see Supplemental File 2). Middle, per cluster fraction of cells from the –E2 vs +E2 samples. Bottom, per cluster distribution of predicted cell cycle state. Points represent individual cells. **(D)** Expression of homologous recombination genes (https://www.genome.jp/entry/hsa03440) from targeted capture panel. *, ANOVA adj.p <0.05 versus Cluster 1. Points represent individual cells. **(E)** Haircut assay from hairpin DNA repair substrates that require activity of the indicated enzymes for editing and sequence readout. ****, ANOVA adj.p <0.0001, –E2 vs +E2. Points represent individual cells. **(F)** Repair of the Abasic hairpin yields two outcomes; APE1-mediated incision at an abasic site is followed by processing by either Polβ (short-patch repair, Abasic.1 - top) or Polδ/β and FEN1 (long-patch repair, Abasic.2 - bottom). *, ANOVA adj.p <0.05 versus Cluster 5. Points represent individual cells.

Rapid NHEJ activation and lack of RAD51 turnover in ILC cells are consistent with HR dysfunction

The depletion of HR proteins associated with MDC1 in ILC cells, coupled with our prior observation that ILC cells show pan-nuclear gH2AX in response to DNA damage without an increase in gH2AX foci (12), are consistent with DNA repair dysfunction but the nature of the dysfunction is unclear. To examine DNA repair signaling further, we induced DNA damage in MM134 ILC cells and examined levels and phosphorylation of key proteins in DNA damage response (DDR) initiation and resolution. Etoposide treatment led to DDR protein phosphorylation, including proteins both upstream of MDC1 (H2AX, ATM, MRN complex proteins) and downstream of MDC1 (CHK1/2, 53BP1, DNA-PKcs) (**Figure 4A**), supporting that initiation of DDR is intact in these cells. Notably, phosphorylation of NHEJ-associated proteins (53BP1, DNA-PKcs) was rapid and seen within 4hrs, while RAD51 turnover associated with HR (31,32) was not apparent in MM134 cells. We next examined induction and resolution of DDR protein phosphorylation in MM134 (ILC) compared to MCF7 (IDC) after etoposide treatment. 53BP1 and DNA-PKcs phosphorylation occurred immediately in ILC cells whereas this was delayed in IDC cells (**Figure 4B**), supporting rapid activation of NHEJ in MM134. In parallel, etoposide treatment decreased levels of RAD51 in MCF7 consistent with RAD51 turnover during HR (33), whereas this was not observed in MM134 out to 48hrs post-damage.

The lack of RAD51 protein turnover may be further supportive of dysfunctional HR-mediated DSBR in ILC cells. Notably, MDC1 plays a central role in the "decision" between HR and NHEJ, and MDC1:RAD51 association was shown to be critical to initiation of HR (33). RAD51 was not detected in our IP/MS studies, so we examined this by co-IP with immunoblotting. We confirmed in MCF7 (IDC) that MDC1 was strongly associated with RAD51, and confirmed the decrease in RAD51 after etoposide treatment (**Figure 4C**). Conversely, we detected minimal MDC1:RAD51 association in MM134 (ILC) and confirmed no decrease in RAD51 after DNA damage. Collectively these data suggest that RAD51 is not effectively engaged in HR, and is consistent with inefficient or dysfunctional HR in ILC cells.

ILC tumor and cell line protein array data are consistent with HR dysfunction

TCGA data also support that RAD51 engagement in DNA repair is dysfunctional in ILC cells. RAD51 is part of the DNA damage response RPPA signature proteins elevated in ILC versus IDC tumors (4,34). RAD51 is elevated in ER+ ILC vs IDC (**Figure 5A**), despite significantly lower *RAD51* mRNA levels in ER+ ILC (**Figure 5B**), suggesting RAD51 is increased post-transcriptionally e.g. dysfunctional post-HR turnover. Further, while RAD51 protein and mRNA levels are positively correlated in ER+ IDC, no correlation is present in ER+ ILC; RAD50 protein/mRNA are positively correlated in both ILC/IDC (**Figure 5C**). Taken together, our data suggest that while DDR initiation and NHEJ are functional in ILC cells, resolution of DSB via HR is inefficient or dysfunctional.

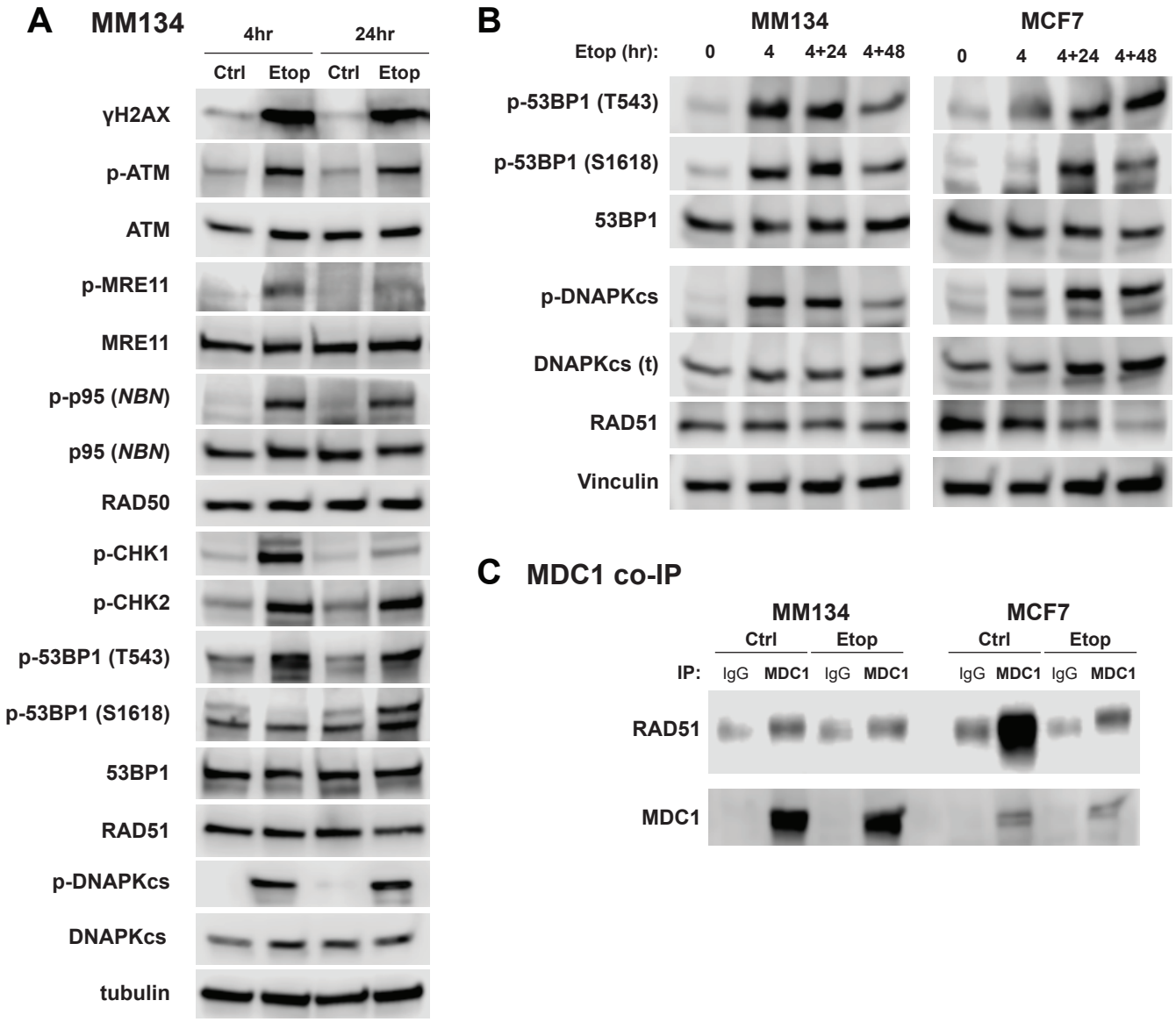
A
MM134
4hr
24hr
Ctrl
Etop
Ctrl
Etop
γH2AX
p-ATM
ATM
p-MRE11
MRE11
p-p95 (NBN)
p95 (NBN)
RAD50
p-CHK1
p-CHK2
p-53BP1 (T543)
p-53BP1 (S1618)
53BP1
RAD51
p-DNAPKcs
DNAPKcs
tubulin
B
MM134
MCF7
Etop (hr):
0
4
4+24
4+48
0
4
4+24
4+48
p-53BP1 (T543)
p-53BP1 (S1618)
53BP1
p-DNAPKcs
DNAPKcs (t)
RAD51
Vinculin
C
MDC1 co-IP
MM134
MCF7
Ctrl
Etop
Ctrl
Etop
IP:
IgG
MDC1
IgG
MDC1
IgG
MDC1
IgG
MDC1
RAD51
MDC1

Figure 4. Activation of HR is limited and delayed in MM134 (ILC) versus MCF7 (IDC) cells. (A) MM134 cells treated with 10μM etoposide for 4 or 24 hours were analyzed by western blot for canonical interactors of MDC1 (yH2AX, ATM, and MRN) and down-stream mediators of canonical MDC1 signaling (CHK1/2, 53BP1, RAD51, and DNAPKcs). **(B)** Western blot comparison of MM134 (ILC) and MCF7 (IDC) for MDC1 interaction of downstream NHEJ (53BP1 and DNAPKcs) vs HR (Rad51) was performed. Increased turnover of RAD51 in MCF7 is suggestive of HR being used to repair etoposide induced double strand breaks. **(C)** Immunoprecipitation of MDC1 in MM134 and MCF7 cells treated with 10μM etoposide. Increased co-IP of RAD51 is observed in MCF7 but not MM134.

In the TCGA analyses of ER+ ILC tumors, the 'Proliferative' mRNA subtype of ILC had an elevated DNA Damage Response (DDR) score based on RPPA analyses (**Figure 5D, left**). The DDR score was similarly elevated in Proliferative ILC relative to Luminal A IDC tumors (**Figure 5D, right**). TCGA initially reported that these Proliferative ILC tumors, which accounted for ~30% of Luminal A ILC, had the poorest outcomes among ILC (2-fold increased risk of recurrence). We examined whether elevated DDR score similarly predicted outcome among ER+ ILC or ER+ IDC in TCGA, and found that high DDR score predicted poorer overall survival in ILC, but not IDC tumors (**Figure 5E**). ILC cell lines mirror the elevated DDR signature observed in Proliferative ILC; in DepMap (35) ILC lines MM134 and CAMA1 had the highest and third-highest DDR score, respectively, among 12 ER+/HER2- models (**Figure 5F**). Similarly, in our RPPA analyses (36), ILC models MM134 and 44PE had elevated DDR scores vs IDC model MCF7 (**Figure 5G**). These data support that DNA repair protein activity has specific implications for ILC tumor biology and patient outcomes, and that ILC cell lines are relevant models to examine DDR function in this context.

ILC cells are sensitive to single-agent PARP inhibitor talazoparib in vitro and in vivo

With evidence that ILC cell lines and tumors present with HR dysfunction, and that MDC1 co-regulator function is linked to reliance PARP-mediated DNA repair, we examined whether ILC cells are sensitive to PARP inhibition. We focused on FDA-approved agent talazoparib, which more potently traps PARP1/2 on DNA relative to olaparib (37). Via live cell Incucyte imaging we found that ILC cell lines MM134 and 44PE are sensitive to low-nanomolar concentrations of talazoparib (**Figure 6A**), similar to MCF-7 but ~10-fold more sensitive than T47D cells. Parallel experiments measuring cell proliferation by dsDNA quantification confirmed low-nanomolar talazoparib sensitivity in ILC cells (**Figure 6B**, **Supplemental Figure 4A**). Notably, both confluence and dsDNA quantification time-courses suggested that the impact of talazoparib treatment on ILC cells manifested at 5-6 days post-treatment, and that surviving IDC cells were likely more viable after longer term talazoparib treatment than ILC cells (**Supplemental Figure 4A-B**). Consistent with this, we assessed cell viability by flow cytometry (propidium iodide and/or annexin V positivity as a marker of non-viable cells) in cells remaining after 7 days treatment. In MCF7 (IDC) cells, talazoparib did not increase cell death compared to control, whereas MM134 (ILC) cells showed a ~12% increase in cell death, consistent with decreased post-treatment viability specifically in ILC cells (**Figure 6C**). To further examine post-treatment cell viability, we washed out drug and re-plated cells after the 7 day treatment, and re-assessed proliferation. ILC cell lines MM134 and 44PE, but not IDC lines MCF7 and T47D, remained significantly growth inhibited after drug washout (**Figure 6D**), suggesting that PARPi treatment had a long-term impact on cell viability specifically in ILC cells.

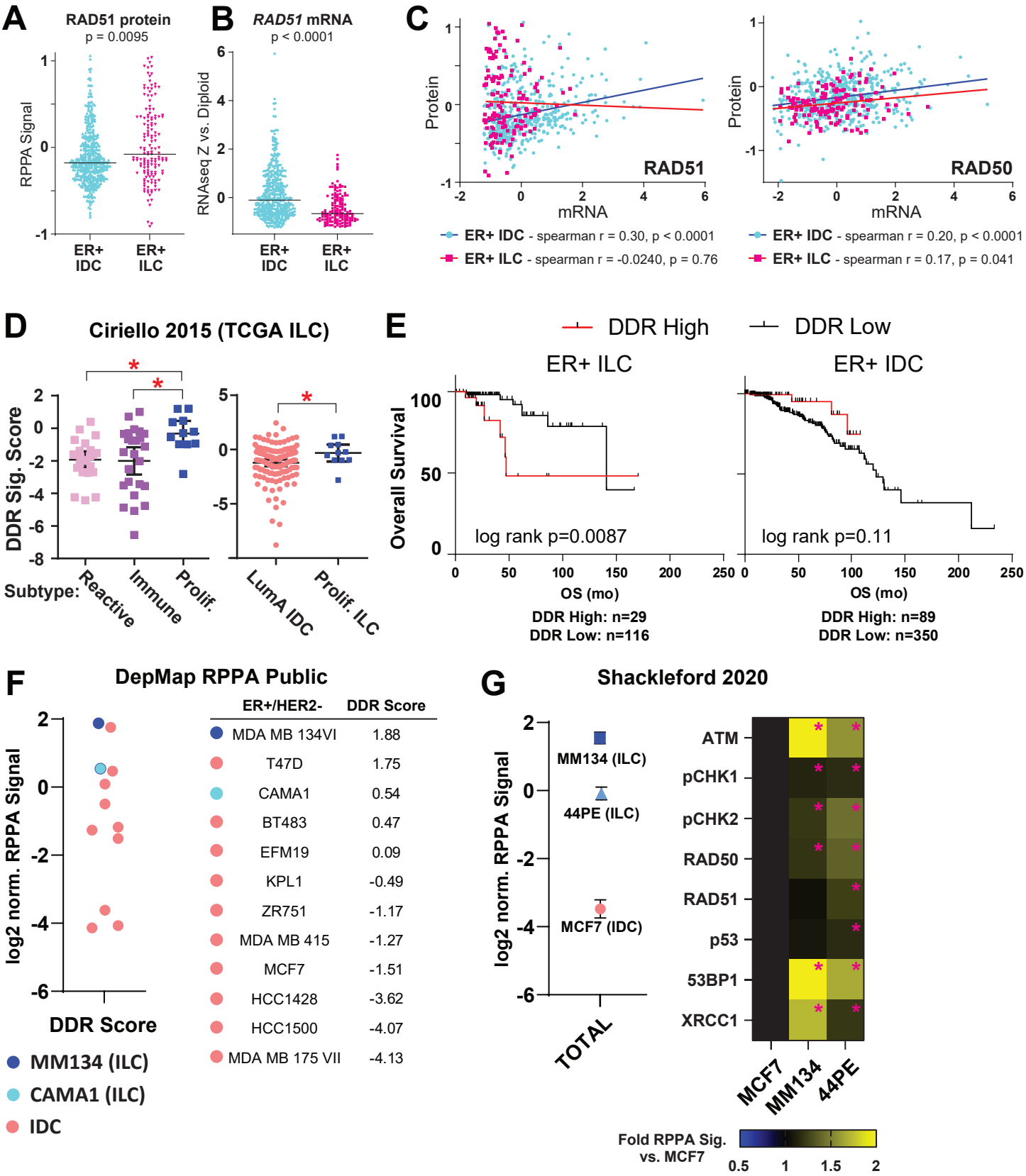
A
RAD51 protein
p = 0.0095
RPPA Signal
ER+ IDC
ER+ ILC
B
RAD51 mRNA
p < 0.0001
RNAseq Z vs. Diploid
ER+ IDC
ER+ ILC
C
Protein
mRNA
RAD51
ER+ IDC - spearman r = 0.30, p < 0.0001
ER+ ILC - spearman r = -0.0240, p = 0.76
RAD50
ER+ IDC - spearman r = 0.20, p < 0.0001
ER+ ILC - spearman r = 0.17, p = 0.041
D
Ciriello 2015 (TCGA ILC)
DDR Sig. Score
Subtype:
Reactive
Immune
Prolif.
LumA IDC
Prolif. ILC
E
DDR High
DDR Low
ER+ ILC
ER+ IDC
Overall Survival
log rank p=0.0087
log rank p=0.11
OS (mo)
DDR High: n=29
DDR Low: n=116
DDR High: n=89
DDR Low: n=350
F
DepMap RPPA Public
log2 norm. RPPA Signal
DDR Score
MM134 (ILC)
CAMA1 (ILC)
IDC
ER+/HER2- DDR Score
MDA MB 134VI 1.88
T47D 1.75
CAMA1 0.54
BT483 0.47
EFM19 0.09
KPL1 -0.49
ZR751 -1.17
MDA MB 415 -1.27
MCF7 -1.51
HCC1428 -3.62
HCC1500 -4.07
MDA MB 175 VII -4.13
G
Shackleford 2020
log2 norm. RPPA Signal
MM134 (ILC)
44PE (ILC)
MCF7 (IDC)
TOTAL
ATM
pCHK1
pCHK2
RAD50
RAD51
p53
53BP1
XRCC1
MCF7
MM134
44PE
Fold RPPA Sig. vs. MCF7
0.5
1
1.5
2

Figure 5. Protein array data are consistent with DNA repair dysfunction in ILC tumors and cell lines. (A-C) mRNA and protein data downloaded from cBio Portal, TCGA Firehose. **(A)** RAD51 reverse phase protein array data, normalized signal. Solid line = median, p value via one-way ANOVA for ILC vs IDC. **(B)** mRNA data, as in (A). **(C)** mRNA Z-score (as in B) vs RPPA normalized signal (as in A). **(D)** Data derived from Ciriello et al, 2015, scores and subtypes as provided in associated supplemental data. **(E)** DDR score re-calculated from RPPA data in cBio portal, see Methods. High vs Low DDR scores separated by top quintile for ILC and IDC separately. Survival data from TCGA PanCancer dataset. **(F)** DDR score calculated as in (E) using DepMap normalized RPPA signal, see Methods. **(G)** Data from Shackleford et al, 2020. Left, points represent mean of biological triplicate ± SD. Right, mean of individual signal, shown as fold change vs MCF7 (IDC). *, ANOVA for sample vs MCF7, adj.p < 0.05.

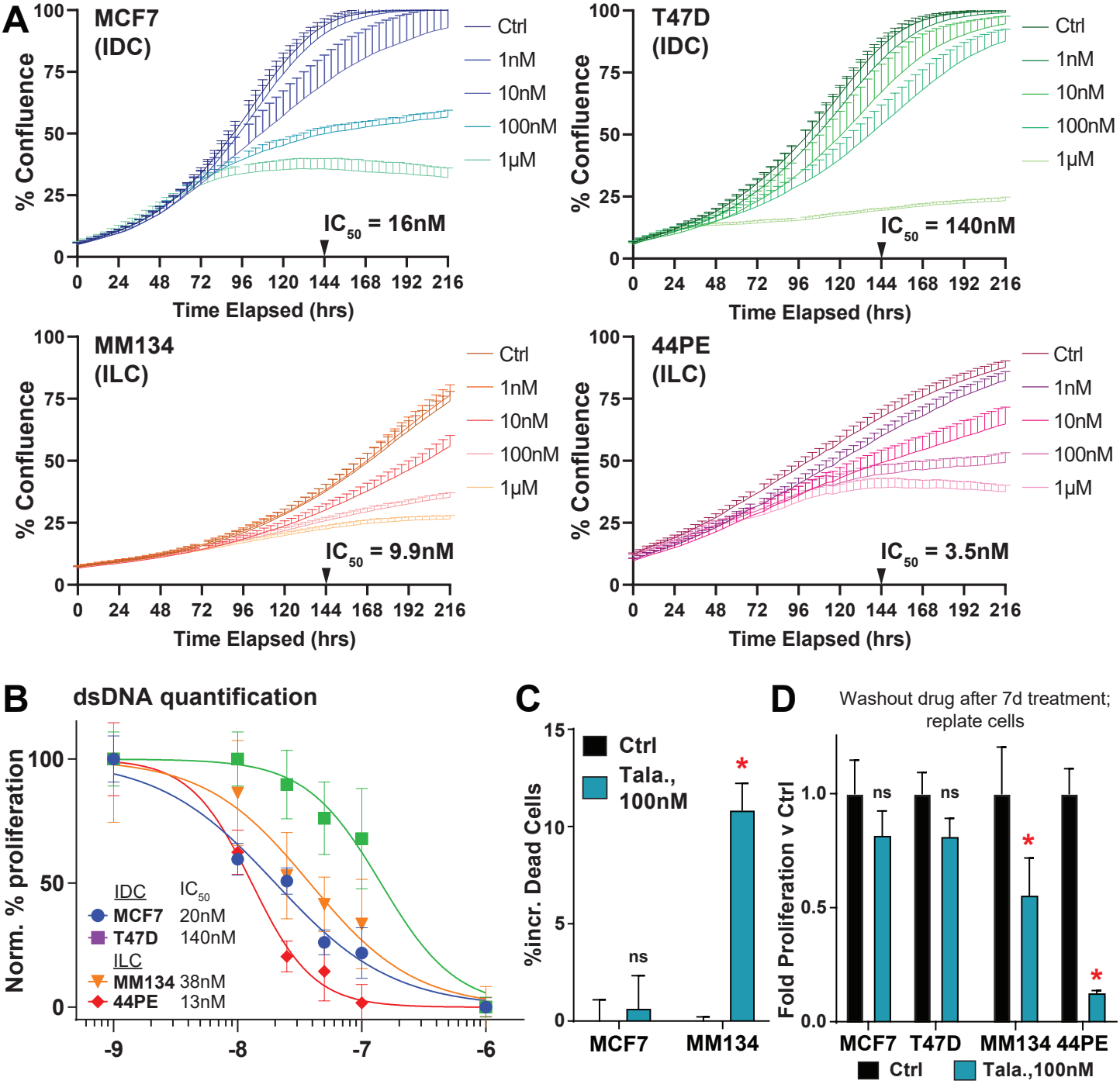
A
MCF7
(IDC)
% Confluence
Time Elapsed (hrs)
Ctrl
1nM
10nM
100nM
1μM
IC50 = 16nM
T47D
(IDC)
IC50 = 140nM
MM134
(ILC)
IC50 = 9.9nM
44PE
(ILC)
IC50 = 3.5nM
B
dsDNA quantification
Norm. % proliferation
IDC
IC50
MCF7 20nM
T47D 140nM
ILC
MM134 38nM
44PE 13nM
C
%incr. Dead Cells
Ctrl
Tala., 100nM
ns
*
MCF7
MM134
D
Washout drug after 7d treatment; replate cells
Fold Proliferation v Ctrl
ns
*
MCF7
T47D
MM134
44PE
Ctrl
Tala.,100nM

Figure 6. ILC cells *in vitro* are sensitive to PARP inhibitor talazoparib. (A) Representative growth curves via confluence in live cell imaging (Incucyte) for ILC vs IDC cells with increasing concentrations of talazoparib. IC_{50} calculated using percent confluence at 144hr post-treatment. Line represents mean confluence of 6 replicates ± SD. **(B)** Proliferation at 7d (168hr) as assessed by dsDNA quantification, shown as normalized % proliferation vs max/min. Points represent mean of 6 replicates ± SD. **(C)** Cells were harvested at 7d (168hr) for flow cytometry. Bars represent mean of total population of PI and/or Annexin V positive cells from 3 replicates ± SD. *, ANOVA, Ctrl v Tala $p<0.05$. **(D)** Proliferation at 7d post drug washout (14d after initial treatment) by dsDNA quantification. Bars represent mean of 6 replicates ± SD. *, ANOVA, Ctrl v Tala $p<0.05$.

We next examined talazoparib efficacy *in vivo* using MM134 mammary fat pad xenograft tumors in female NSG mice. 20 mice were injected with $5x10^6$ MM134 cells in matrigel bilaterally at the #4 mammary fat pad, and mice were supplemented with 30μM estradiol in drinking water to support tumor growth. Treatments were initiated at day 27 post-tumor challenge with >25% of tumors >$100mm^3$. n=5 mice per arm received vehicle (vehicle gavage, see Methods), 0.33mg/kg talazoparib (5d/w p.o.) for 3 weeks, 0.33mg/kg talazoparib for 6 weeks, or fulvestrant (5mg/kg s.c. weekly) for 6 weeks; tumors were tracked until all vehicle control mice reached humane study endpoints (day 79). Of note, the 6-week talazoparib arm was lost at day 72 due to a cage flood and data were censored. Neither talazoparib nor fulvestrant had a significant impact on mouse weight gain over the course of the study (**Supplemental Figure 5A**).

Single agent talazoparib treatment for either 3 or 6 weeks significantly suppressed tumor growth versus control (ANOVA Vehicle vs 3wk Tal, $p<0.0001$), and outperformed fulvestrant in reducing tumor growth (ANOVA Fulvestrant vs 3wk Tal, $p=0.0035$) (**Figure 7A**). Fulvestrant provided an initial growth suppression, but tumors continued to grow on treatment. Conversely, though talazoparib treated tumors were larger than at study initiation (3wk Tal: ~2.9-fold increase at endpoint, paired t-test $p=0.002$), growth inhibition was durable and tumors did not significantly increase in volume between treatment completion and study endpoint (day 48 vs day 79, paired t-test $p=0.11$). Accordingly, talazoparib improved survival (as defined by humane study endpoints) versus vehicle (log rank $p=0.0027$) or versus fulvestrant (log rank $p=0.0126$) (**Figure 7B**). This durable growth suppression of MM134 *in vivo* after talazoparib treatment mirrors our *in vitro* observations and supports that ILC cells are uniquely sensitive to PARPi.

DISCUSSION

Patients diagnosed with ILC are faced with distinct treatment and clinical management challenges, in part related to uniquely poor long-term outcomes, controversy around the efficacy of anti-estrogens, and a lack of biomarker and therapy strategies based on ILC biology. Toward better understanding estrogen and anti-estrogen response in ILC, we previously identified that the DNA repair protein MDC1 has novel ER co-regulator activity in ILC cells that mediates estrogen response and anti-estrogen resistance, yet is associated with putative DNA repair dysfunction (12). In the present study, we profiled the MDC1 interactome to characterize MDC1 association with DNA repair vs transcriptional or epigenetic partners in IDC versus ILC cells. In the latter, MDC1 associations with homologous recombination proteins were depleted in ILC cells, mirroring that observed in *BRCA2*-mutant IDC cells. Using single-cell transcriptomics paired with DNA repair activity measurement with the 'Haircut' assay, we found that ER:MDC1 gene regulation activity was associated with an upregulation of PARP-mediated repair pathways, specifically increased activity of base excision repair and APE1. Collectively, these data support that ILC cells have a previously unappreciated form of DNA repair

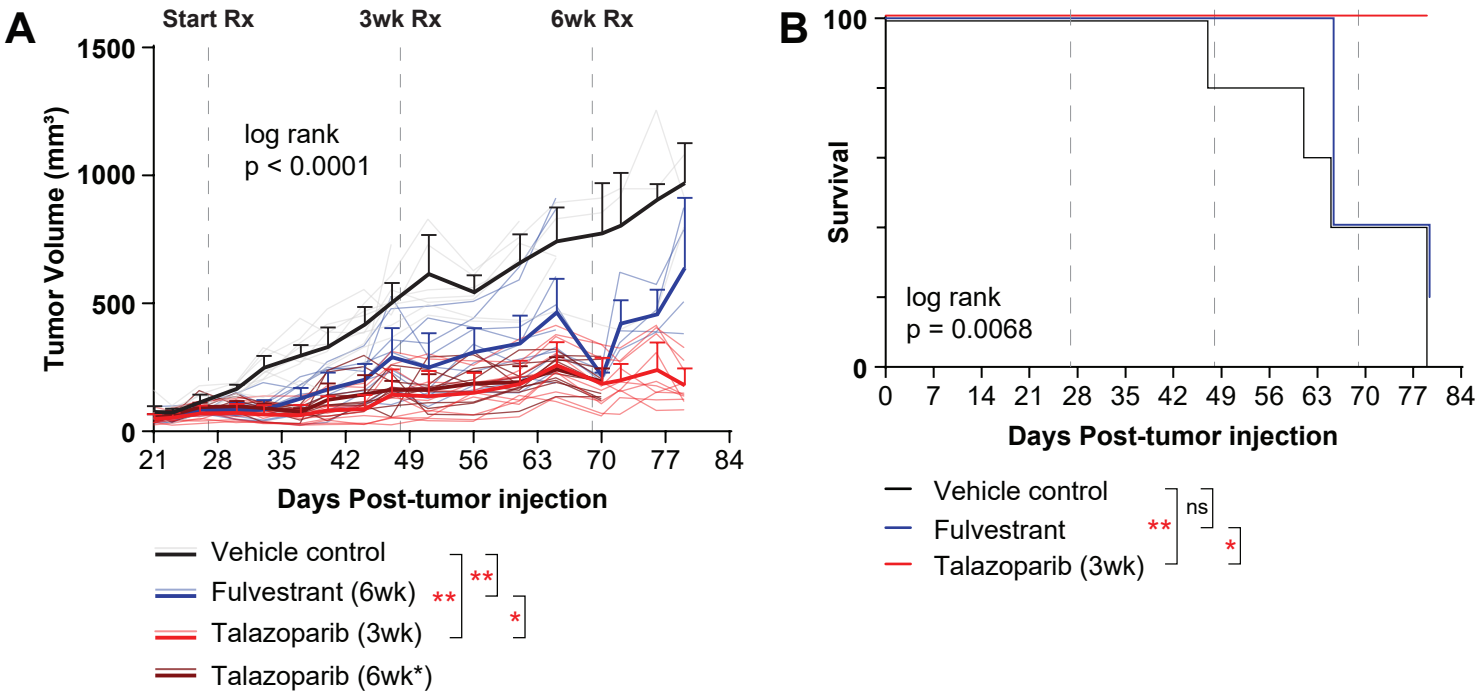
A
Start Rx
3wk Rx
6wk Rx
Tumor Volume (mm³)
1500
1000
500
0
log rank
p < 0.0001
21
28
35
42
49
56
63
70
77
84
Days Post-tumor injection
Vehicle control
Fulvestrant (6wk)
Talazoparib (3wk)
Talazoparib (6wk*)
**
**
*
B
100
Survival
0
log rank
p = 0.0068
0
7
14
21
28
35
42
49
56
63
70
77
84
Days Post-tumor injection
Vehicle control
Fulvestrant
Talazoparib (3wk)
ns
**
*

Figure 7. Talazoparib causes sustained growth suppression in MM134 xenograft tumors. (A) Tumor volumes as faded lines are from individual tumors (Control: 9 tumors in 5 mice; other models: 10 tumors in 5 mice, each). Solid lines represent mean of tumors still on study + SD. Statistics shown - 2-way ANOVA treatment effect. **, $p<0.0001$. *, $p=0.0035$. Vertical dashed lines represent treatment initiation and completion times. **(B)** Survival as defined by humane endpoint, i.e. any tumor measurement reaching 15mm. 6wk talazoparib not shown, but no mice on that arm reached the survival endpoint at the time the group was lost (see text). Statistics shown - 2-way ANOVA treatment effect. **, $p=0.0027$. *, $p=0.013$.

dysfunction, and we tested whether this dysfunction could be exploited using FDA-approved PARPi talazoparib. Both *in vitro* and *in vivo*, ILC cells were sensitive to talazoparib, which caused durable suppression of cell/tumor growth after treatment cessation. Understanding how MDC1 underpins ILC-specific ER functions and DNA repair dysfunction offers a path toward ILC precision therapies based on identifying tumors where ER:MDC1 activity indicates PARPi sensitivity.

While our data shows that MDC1 in ILC cells associates with a broad range of epigenomic partners, which may mediate gene regulation, the mechanisms underlying MDC1-ER co-regulation specifically in ILC cells requires further investigation. MDC1 is well understood to be critical in propagating and regulating DNA repair downstream of binding γH2AX after DNA damage (13,14,38). More recently, MDC1 has been associated with maintaining chromatin integrity during transcription including a potential role for MDC1 in RNA PolII elongation (24,28). In this latter context it is yet unclear whether MDC1 is binding at promoters in response to transcription-induced DNA damage or directly binding transcriptional machinery. Recent work suggests that MDC1 is constitutively associated with chromatin (25), supporting that MDC1 does not only bind chromatin in response to DNA damage. Importantly, Heyza et al (25) and Salguero et al (38) showed that the disordered PST domain of MDC1 mediates chromatin binding independent of γH2AX binding (via the BRCT domain), via the PST domain binding directly to histones (38) though MDC1 may directly bind DNA (39). MDC1 genome-wide cistrome data would offer critical insight to potentially distinct modes of MDC1 binding to chromatin, but the largely disordered nature of MDC1 may create technical challenges with ChIP-seq, and MDC1 genomic binding to date is only inferred from MRN complex binding (24). Inference via MRN likely provides an incomplete picture of MDC1 genomic binding since we found minimal MRN:MDC1 association in ILC cells. Notably, transcriptional activities of MDC1 investigated to date are primarily associated with its DNA repair activity – our work suggests that the co-regulator functions of MDC1 in ILC are yet distinct. We previously showed that MDC1 suppression in MM134 cells inhibited ER function but had no effect on androgen receptor activity (12), suggesting that MDC1 is specifically co-regulating ER and not broadly critical for transcription or gene regulation. Similarly, MDC1 suppression in ILC cells caused cell cycle arrest (12), whereas in IDC cells and other models, MDC1 suppression abrogates cell cycle checkpoints. We also saw via RNAseq that MDC1 knockdown dysregulated DNA repair pathways in IDC cells, but not ILC cells (12). Ongoing work in our group is examining whether MDC1 indeed has novel activity or function in ILC, and/or whether ER in ILC is uniquely able to exploit MDC1 chromatin binding, and how this is related to or caused by MDC1 dysfunction in DNA repair.

ILC are not associated with typical features of DNA repair deficiency or sensitivity to DNA damage – in addition to the limited genomic scars of overt HR deficiency and depletion of germline *BRCA1/2* and *TP53* mutations in ILC (18–20), ILC generally have a poor response to chemotherapy (2,40). However, our data taken together with observations in the literature suggest that some ILC may present with DNA repair dysfunction

that does not manifest as HR deficiency as currently understood. The elevated DNA damage response signature identified in Proliferative ILC in TCGA supports that DDR plays a distinct role in ILC etiology, particularly aggressive ILC associated with poor outcomes. The mechanistic significance of the elevated DDR signature is unknown, but the lack of RAD51 turnover in response to etoposide that we observed suggests that elevated DDR protein levels could be due to inefficient or dysfunctional initiation, propagation, or resolution of DDR in response to DNA damage. Rather than resulting in large genomic scars, this dysfunction may result in increased tumor mutational burden (TMB) that is progressive with ILC recurrence and metastasis - recent analysis of Foundation Medicine sequencing data showed that ILC has an elevated TMB compared other ER+ breast cancers. Sokol et al (41) reported that though high TMB was uncommon is primary ER+ breast cancer, it was more frequent in ILC (2.1%) than IDC (0.8%); 17% of ILC vs 14.6% of IDC were classified as TMB medium or high. TMB was increased in metastatic ER+ ILC (mILC), as 8.9% of mILC vs 1.5% of metastatic IDC (mIDC) had high TMB (p=0.0016), and 37% of mILC vs 25% of mIDC had medium or high TMB (p=0.013). We noted that in ER+ ILC in TCGA, increased TMB as reported in cBio Portal was associated with high DDR score (as in Figure 5, p=0.038, not shown), supporting that DNA repair dysfunction in ILC manifests as increased TMB. Taken together with our *in vitro* and *in vivo* data showing that talazoparib may effectively exploit DNA repair dysfunction in ILC cells, at least a subset of patients with ILC may benefit from treatment with PARPi. Owing to the paucity of germline *BRCA1/2*-mutant ILC, clinical data on PARPi response for ILC are limited. The phase III olaparib trial OlympiAD did not report tumor histology in initial results or subgroup analyses, and the two largest breast cancer trials of talazoparib reported to date (EMBRACA (42) and ABRAZO (43)) did not report tumor histology. A pilot neoadjuvant talazoparib study (44) included one germline *BRCA2*-mutant patient with ER+ ILC which had a pathologic complete response to talazoparib, but the extended version of the trial, NEOTALA, did not report tumor histology (45). Defining biomarkers for DNA repair activity and/or MDC1 repair vs genomic activity in ILC is critical to better understand the scope of DNA repair dysfunction in ILC and to design effective trials for talazoparib in ILC.

It is important to consider that though *TP53* mutations are uncommon in ILC, the cell line models used in our studies do carry *TP53* mutations, which is typical of cancer cell lines including ILC (46–48). However, as noted above, MM134 and 44PE do mirror 'Proliferative' ILC regarding the elevated DNA damage response protein signature, and recent multi-omic profiling of putative ILC models supports that MM134 and 44PE are suitable models of ER+/luminal ILC (48). Additionally, future studies must incorporate anti-estrogen-resistant ILC, as we previously identified altered DNA repair signaling in long-term estrogen-deprived (LTED, modeling aromatase inhibitor resistance (49)) ILC models at the transcriptomic level (50) and signaling level (36), which will likely impact assessment of DNA repair dysfunction and PARPi response.

It is becoming increasingly urgent to develop treatment strategies centered on a differential diagnosis of breast cancer of no special type (i.e. IDC), versus a diagnosis of ILC. In contrast to the lack of histology

information in most trials, a recent series of clinical studies are enriching for or specifically enrolling patients with ILC (e.g. ROSALINE (51), GELATO (52), NCT02206984). New prognostic signatures developed based on ILC tumors have been reported (53), and pre-clinical studies focusing on ILC models are beginning to identify and define ILC-specific biology toward ILC-tailored treatments (12,50,54–56). Our data advance this paradigm of targeting ILC biology, and show that ILC-specific association between ER and MDC1 creates a new context for ER and MDC1 function in ILC, yet creates a putative synthetic vulnerability, i.e. a DNA repair dysfunction that may be exploitable with PARPi.

MATERIALS AND METHODS

Cell culture

MDA MB 134VI (MM134; ATCC HTB-23) and SUM44PE (44PE; Asterand/BioIVT) were maintained as described (57). HCC1428 (ATCC CRL-2327), MCF7 (Rae Lab, U. Michigan) and T47D (Sartorius Lab, U. Colorado) were maintained as described (12). 293FT cells (Invitrogen) were maintained according to manufacturer directions. Cells were incubated at 37°C in 5% CO_2. All lines were regularly confirmed mycoplasma negative (MycoAlert, Lonza), and authenticated by STR profiling at the U. Colorado Anschutz Tissue Culture Core. Estradiol (E2) was from Sigma; ICI 182780 (fulvestrant; fulv) was from Tocris Biosciences. Etoposide and talazoparib (BMN-673) were from Cayman Chemical Company. Small molecules were dissolved in ethanol, and vehicle treatments use 0.01-0.1% EtOH *in vitro*.

MDC1 co-immunoprecipitation and mass spectrometry

Immuno-precipitation (IP) was performed as previously described (12). Briefly, nuclear extract (NE) was prepared from successive hypotonic/hypertonic washes and lysing, then utilized for immunoprecipitation. 10µg antibody was used with NE for immunoprecipitation. Jackson ImmunoResearch Chromapure Mouse IgG was used for control. α-MDC1 (Sigma M2444) was used for MDC1 IP. NE was incubated with antibody overnight at 4°C with rotation, then extracted with magnetic A/G beads for 4hr at 4°C with rotation. For IP/mass spectrometry, bead-complexes were submitted intact to the Mass Spectrometry Core Facility at the University of Colorado – Boulder for sample preparation and analysis, using an Orbitrap nanoLC-MS. For IP followed by immunoblot, protein complexes were eluted by re-suspending beads in Laemmli-based buffer.

MDC1-IP/MS iBAQ values were used for comparison. IgG iBAQ values were subtracted as background from MDC1-IP values for all proteins. Only proteins enriched (i.e. background subtracted iBAQ > 0) were included in subsequent analyses. Genes present in GO genesets GO:0006397, GO:0000398, GO:0000377, GO:0006364, and GO:0042254 (related to RNA metabolism, see Supplemental File 1) were

excluded from analysis as indicated in the text. MDC1 co-immunoprecipitated genes in 293FT (n=1666) were compared to Salifou et al (24) for validation of our IP/MS method. Enriched gene lists for each cell line were analyzed using EnrichR (58) for gene set enrichment analysis. Hierarchical clustering of gene sets was performed using Morpheus (https://software.broadinstitute.org/morpheus).

Single cell transcriptomics and Haircut analyses

MM134 cells were hormone-deprived in medium supplemented with charcoal-stripped FBS as previously described (59), then treated with vehicle (0.01% ethanol) or 100pM estradiol for 24hrs. After treatment, single cell suspensions were prepared according to 10X Genomics recommendations, and as described (29,30). Whole transcriptome and Haircut libraries were prepared as described (29,30), and separate targeted capture libraries were prepared according to the manufacturer's instructions (https://www.10xgenomics.com/products/targeted-gene-expression). Supplemental File 2 includes workflow information and normalized gene expression data for the targeted capture panel and Haircut probes, with single-cell annotation for clustering, cell cycle prediction, and ER target genes scores, and is available at: https://osf.io/rw2n6. Raw data will be made available upon submission for publication, or upon request.

Immunoblotting

Cells were seeded in 12-well plates for ~80% confluence (MM134: 800k/well; MCF7: 320k/well) and treated as indicated prior to lysis with RIPA buffer (Thermo Pierce). Primary antibodies were diluted to manufacturer recommended concentrations, in TBS + 0.05% Tween-20. Membranes were imaged on LiCor C-DiGit blot scanner. Primary antibodies for immunoblots were: phospho-Histone H2A.X (Ser139)(20E3) (Cell Signaling Technology #9718); ATM (D2E2) (Cell Signaling Technology #2873); Phospho-ATM (Ser1981)(D6H9)(Cell Signaling Technology #5883); MRE11 (31H4)(Cell Signaling Technology #4847); phosph-MRE11 (Ser676)(Cell Signaling Technology #4859); p95/NBS1 (NBN) (D6J5I)(Cell Signaling Technology #14956); phospho-p95/NBS1 (NBN)(Ser343)(Cell Signaling Technology #3001); Rad50 (Cell Signaling Technology #3427); phospho-CHK1 (Ser345)(133D3)(Cell Signaling Technology #2348); phospho-CHK2 (Thr68)(C13C1)(Cell Signaling Technology #2197); 53BP1 (E7N5D) XP (Cell Signaling Technology #88439); phospho-53BP1 (Ser1618)(D4H11)(Cell Signaling Technology #6209); phospho-53BP1 (Thr543)(Cell Signaling Technology #3428); Rad51 (D4B10)(Cell Signaling Technology #8875); DNA-PKcs (3H6)(Cell Signaling Technology #12311); phospho-DNA-PKcs (Ser2056)(E9J4G)(Cell Signaling Technology #68716); α/β-Tubulin (Cell Signaling Technology #2148); Vinculin (E1E9V) XP (Cell Signaling Technology #13901); MDC1 (MDC1-50)(Sigma-Aldrich M2444).

DNA damage response score

DNA damage response (DDR) scores were determined from public RPPA data for breast cancer cell lines (35), our cell line data set (36), or the TCGA Firehose Legacy (60) dataset by summing normalized log2 RPPA signal for targets defined by Akbani et al (53BP1, ATM, pCHK1, pCHK2, p53, RAD50, RAD51, XRCC1). This DDR score originally included BRCA2, KU80/XRCC5, and MRE11, but data for these targets are not available with RPPA data from data sources herein and they were excluded from our analyses.

Cell proliferation and viability

Total double-stranded DNA was quantified by Hoechst 33258 fluorescence as described (61), as a surrogate for cell number. Apoptosis was measured using the Invitrogen eBioscience Annexin V Apoptosis detection kit (Cat # 50-929-7) according to manufacturer instructions. Flow cytometric analysis was performed using a Beckman Coulter Gallios561 cytometer (Indianapolis, IN, USA) at the U. Colorado Cancer Center Flow Cytometry Shared Resource Data was analyzed using Kaluza Analysis Software v2.1 (Beckman Coulter). Live cell analysis was performed using an S3 Incucyte (Sartorius, Bohemia, NY, USA) with the U. Colorado Cancer Center Cell Technologies Shared Resource. MCF7 ($2x10^3$ cells per well), T47D ($3x10^3$ cells per well), MM134 ($2x10^4$ cells per well), and 44PE ($1.5x10^4$ cells per well) were plated in a 96-well format. 24 hours after plating, cells were treated with the noted concentrations of talazoparib and placed in the S3 Incucyte for 216 hours. For analysis, a confluence phase mask was used to determine relatively confluency. Alternatively, cells were pre-treated with talazoparib for 7 days prior to re-plating in the 96-well format and analysis.

Animals and xenograft treatment studies

All animal studies were performed in in AALAC-approved facility with approval of the University of Colorado – Anschutz Medical Center Institutional Animal Care and Use Committee (IACUC). 6-8 week female NSG (NOD.Cg-*Prkdc*^{scid} *Il2rg*^{tm1Wjl}/SzJ; Jackson Laboratory strain 005557) mice were used for all experiments. Five mice per group were used for all *in vivo* experiments.

One week prior to tumor challenge, mice were initiated on 30µM β-estradiol (E2) supplemented in the drinking water. Mice were allowed to drink and eat ad libitum for the duration of the study. Mice were weighed weekly as weight loss >10% was used as an indicator of acute toxicity. For tumor challenge, tumor cells were diluted in a 50/50 mixture of HBSS and phenol red-free LDEV-free Matrigel (Corning; Corning NY, USA). Mice were anesthetized with isoflurane, abdomen shaved, and challenged with $5x10^6$ MM134 cells in the bilateral #4 mammary fat pads. Tumor volume was calculated using the formula: $V = (S^2 \text{ x } L) / 2$, where V = volume, L = Longest tumor diameter, and S = shortest tumor diameter. Treatment with fulvestrant (5 mg/kg, diluted in 10% ethanol and 90% peanut oil, administered subcutaneously weekly) or talazoparib (0.33 mg/kg, diluted in 4% DMSO, 30% PEG300 (Sigma-Aldrich), and 66% water, administered by oral gavage daily except for weekends) was initiated when >25% of tumors exceeded ~$100mm^3$. Tumors were measured twice weekly

and mice were weighed weekly. Mice were euthanized when any tumor dimension reached 15mm in the longest diameter as defined humane endpoints.

Software

Graphs were prepared with Graphpad Prism software v10.0 (GraphPad Software, Boston, MA, USA).

REFERENCES

1. Sikora MJ, Jankowitz RC, Dabbs DJ, Oesterreich S. Invasive lobular carcinoma of the breast: patient response to systemic endocrine therapy and hormone response in model systems. Steroids. Elsevier Inc.; 2013;78:568–75.

2. Mouabbi JA, Hassan A, Lim B, Hortobagyi GN, Tripathy D, Layman RM. Invasive lobular carcinoma: an understudied emergent subtype of breast cancer. Breast Cancer Res Treat. Springer US; 2022;193:253–64.

3. McCart Reed AE, Kalinowski L, Simpson PT, Lakhani SR. Invasive lobular carcinoma of the breast: the increasing importance of this special subtype. Breast Cancer Res BCR. Breast Cancer Research; 2021;23:6–6.

4. Ciriello G, Gatza ML, Beck AH, Wilkerson MD, Rhie SK, Pastore A, et al. Comprehensive Molecular Portraits of Invasive Lobular Breast Cancer. Cell. 2015;163:506–19.

5. Arpino G, Bardou VJ, Clark GM, Elledge RM. Infiltrating lobular carcinoma of the breast: tumor characteristics and clinical outcome. Breast Cancer Res BCR. 2004;6:R149-56.

6. Rakha EA, El-Sayed ME, Powe DG, Green AR, Habashy H, Grainge MJ, et al. Invasive lobular carcinoma of the breast: response to hormonal therapy and outcomes. Eur J Cancer Oxf Engl 1990. 2008;44:73–83.

7. Chen Z, Yang J, Li S, Lv M, Shen Y, Wang B, et al. Invasive lobular carcinoma of the breast: A special histological type compared with invasive ductal carcinoma. PloS One. 2017;12:e0182397–e0182397.

8. Mathew A, Rajagopal PS, Villgran V, Sandhu GS, Jankowitz RC, Jacob M, et al. Distinct Pattern of Metastases in Patients with Invasive Lobular Carcinoma of the Breast. Geburtshilfe Frauenheilkd. 2017;77:660–6.

9. Metzger Filho O, Giobbie-Hurder A, Mallon E, Gusterson B, Viale G, Winer EP, et al. Relative Effectiveness of Letrozole Compared With Tamoxifen for Patients With Lobular Carcinoma in the BIG 1-98 Trial. J Clin Oncol Off J Am Soc Clin Oncol. 2015;33:2772–9.

10. Riba LA, Russell T, Alapati A, Davis RB, James TA. Characterizing Response to Neoadjuvant Chemotherapy in Invasive Lobular Breast Carcinoma. J Surg Res. Elsevier Inc; 2019;233:436–43.

11. Truin W, Voogd AC, Vreugdenhil G, van der Heiden-van der Loo M, Siesling S, Roumen RM. Effect of adjuvant chemotherapy in postmenopausal patients with invasive ductal versus lobular breast cancer. Ann Oncol. 2012;23:2859–65.

12. Sottnik JL, Bordeaux EK, Mehrotra S, Ferrara SE, Goodspeed AE, Costello JC, et al. Mediator of DNA Damage Checkpoint 1 (MDC1) Is a Novel Estrogen Receptor Coregulator in Invasive Lobular Carcinoma of the Breast. Mol Cancer Res MCR. 2021;19:1270–82.

13. Jungmichel S, Stucki M. MDC1: The art of keeping things in focus. Chromosoma. 2010;119:337–49.

14. Coster G, Goldberg M. The cellular response to DNA damage: a focus on MDC1 and its interacting proteins. Nucl Austin Tex. 2010;1:166–78.

15. Ruff SE, Logan SK, Garabedian MJ, Huang TT. Roles for MDC1 in cancer development and treatment. DNA Repair. 2020;95:102948–102948.

16. Lou Z, Minter-Dykhouse K, Franco S, Gostissa M, Rivera MA, Celeste A, et al. MDC1 maintains genomic stability by participating in the amplification of ATM-dependent DNA damage signals. Mol Cell. 2006;21:187–200.

17. Meyer B, Voss K-O, Tobias F, Jakob B, Durante M, Taucher-Scholz G. Clustered DNA damage induces pan-nuclear H2AX phosphorylation mediated by ATM and DNA-PK. Nucleic Acids Res. 2013;41:6109–18.

18. Dossus L, Benusiglio PR. Lobular breast cancer: incidence and genetic and non-genetic risk factors. Breast Cancer Res BCR. BioMed Central; 2015;17:37–37.

19. Ditchi Y, Broudin C, El Dakdouki Y, Muller M, Lavaud P, Caron O, et al. Low risk of invasive lobular carcinoma of the breast in carriers of BRCA1 (hereditary breast and ovarian cancer) and TP53 (Li-Fraumeni syndrome) germline mutations. Breast J. 2019;25:16–9.

20. Yadav S, Hu C, Nathanson KL, Weitzel JN, Goldgar DE, Kraft P, et al. Germline Pathogenic Variants in Cancer Predisposition Genes Among Women With Invasive Lobular Carcinoma of the Breast. J Clin Oncol Off J Am Soc Clin Oncol. 2021;39:3918–26.

21. Cao L, Basudan A, Sikora MJMJ, Bahreini A, Tasdemir N, Levine KMKM, et al. Frequent amplifications of ESR1, ERBB2 and MDM4 in primary invasive lobular breast carcinoma. Cancer Lett. 2019;461:21–30.

22. Gupta R, Somyajit K, Narita T, Maskey E, Stanlie A, Kremer M, et al. DNA Repair Network Analysis Reveals Shieldin as a Key Regulator of NHEJ and PARP Inhibitor Sensitivity. Cell. 2018;173:972-988.e23.

23. Su D, Ma S, Shan L, Wang Y, Wang Y, Cao C, et al. Ubiquitin-specific protease 7 sustains DNA damage response and promotes cervical carcinogenesis. J Clin Invest. 2018;128:4280–96.

24. Salifou K, Burnard C, Basavarajaiah P, Grasso G, Helsmoortel M, Mac V, et al. Chromatin-associated MRN complex protects highly transcribing genes from genomic instability. Sci Adv. 2021;7:eabb2947.

25. Heyza JR, Mikhova M, Bahl A, Broadbent DG, Schmidt JC. Systematic analysis of the molecular and biophysical properties of key DNA damage response factors. eLife. 2023;12:e87086.

26. Sigismondo G, Arseni L, Palacio-Escat N, Hofmann TG, Seiffert M, Krijgsveld J. Multi-layered chromatin proteomics identifies cell vulnerabilities in DNA repair. Nucleic Acids Res. 2023;51:687–711.

27. Ichijima Y, Ichijima M, Lou Z, Nussenzweig A, Camerini-Otero RD, Chen J, et al. MDC1 directs chromosome-wide silencing of the sex chromosomes in male germ cells. Genes Dev. 2011;25:959–71.

28. Pappas G, Munk SHN, Watanabe K, Thomas Q, Gál Z, Gram HH, et al. MDC1 maintains active elongation complexes of RNA polymerase II. Cell Rep. 2023;42:111979.

29. Richer AL, Riemondy KA, Hardie L, Hesselberth JR. Simultaneous measurement of biochemical phenotypes and gene expression in single cells. bioRxiv [Internet]. 2019;820233. Available from: https://www.biorxiv.org/content/10.1101/820233v1

30. Richer AL, Riemondy KA, Hardie L, Hesselberth JR. Simultaneous measurement of biochemical phenotypes and gene expression in single cells. Nucleic Acids Res. 2020;48:e59–e59.

31. Inano S, Sato K, Katsuki Y, Kobayashi W, Tanaka H, Nakajima K, et al. RFWD3-Mediated Ubiquitination Promotes Timely Removal of Both RPA and RAD51 from DNA Damage Sites to Facilitate Homologous Recombination. Mol Cell. 2017;66:622-634.e8.

32. Antoniuk-Majchrzak J, Enkhbaatar T, Długajczyk A, Kaminska J, Skoneczny M, Klionsky DJ, et al. Stability of Rad51 recombinase and persistence of Rad51 DNA repair foci depends on post-translational modifiers, ubiquitin and SUMO. Biochim Biophys Acta Mol Cell Res. 2023;1870:119526.

33. Zhang J, Ma Z, Treszezamsky A, Powell SN. MDC1 interacts with Rad51 and facilitates homologous recombination. Nat Struct Mol Biol. 2005;12:902–9.

34. Akbani R, Ng PKS, Werner HMJ, Shahmoradgoli M, Zhang F, Ju Z, et al. A pan-cancer proteomic perspective on The Cancer Genome Atlas. Nat Commun. 2014;5:3887–3887.

35. Tsherniak A, Vazquez F, Montgomery PG, Weir BA, Kryukov G, Cowley GS, et al. Defining a Cancer Dependency Map. Cell. 2017;170:564-576.e16.

36. Shackleford MT, Rao DM, Bordeaux EK, Hicks HM, Towers CG, Sottnik JL, et al. Estrogen Regulation of mTOR Signaling and Mitochondrial Function in Invasive Lobular Carcinoma Cell Lines Requires WNT4. Cancers [Internet]. 2020;12. Available from: http://www.ncbi.nlm.nih.gov/pubmed/33053661

37. Cortesi L, Rugo HS, Jackisch C. An Overview of PARP Inhibitors for the Treatment of Breast Cancer. Target Oncol. 2021;16:255–82.

38. Salguero I, Belotserkovskaya R, Coates J, Sczaniecka-Clift M, Demir M, Jhujh S, et al. MDC1 PST-repeat region promotes histone H2AX-independent chromatin association and DNA damage tolerance. Nat Commun. Springer US; 2019;10:5191–5191.

39. Ozaki T, Nagase T, Ichimiya S, Seki N, Ohiri M, Nomura N, et al. NFBD1/KIAA0170 is a novel nuclear transcriptional transactivator with BRCT domain. DNA Cell Biol. 2000;19:475–85.

40. Thomas M, Kelly ED, Abraham J, Kruse M. Invasive lobular breast cancer: A review of pathogenesis, diagnosis, management, and future directions of early stage disease. Semin Oncol. Elsevier Inc.; 2019;46:121–32.

41. Sokol ES, Feng YX, Jin DX, Basudan A, Lee AV, Atkinson JM, et al. Loss of function of NF1 is a mechanism of acquired resistance to endocrine therapy in lobular breast cancer. Ann Oncol Off J Eur Soc Med Oncol. 2019;30:115–23.

42. Litton JK, Rugo HS, Ettl J, Hurvitz SA, Gonçalves A, Lee K-H, et al. Talazoparib in Patients with Advanced Breast Cancer and a Germline BRCA Mutation. N Engl J Med. 2018;379:753–63.

43. Turner NC, Telli ML, Rugo HS, Mailliez A, Ettl J, Grischke E-M, et al. A Phase II Study of Talazoparib after Platinum or Cytotoxic Nonplatinum Regimens in Patients with Advanced Breast Cancer and Germline BRCA1/2 Mutations (ABRAZO). Clin Cancer Res Off J Am Assoc Cancer Res. 2019;25:2717–24.

44. Litton JK, Scoggins ME, Hess KR, Adrada BE, Murthy RK, Damodaran S, et al. Neoadjuvant Talazoparib for Patients With Operable Breast Cancer With a Germline BRCA Pathogenic Variant. J Clin Oncol Off J Am Soc Clin Oncol. 2020;38:388–94.

45. Litton JK, Beck JT, Jones JM, Andersen J, Blum JL, Mina LA, et al. Neoadjuvant Talazoparib in Patients With Germline BRCA1/2 Mutation-Positive, Early-Stage Triple-Negative Breast Cancer: Results of a Phase II Study. The Oncologist. 2023;28:845–55.

46. Sflomos G, Schipper K, Koorman T, Fitzpatrick A, Oesterreich S, Lee AV, et al. Atlas of Lobular Breast Cancer Models: Challenges and Strategic Directions. Cancers. 2021;13:1–35.

47. Bahnassy S, Sikora MJ, Riggins RB. Unlocking the Mysteries of Lobular Breast Cancer Biology Needs the Right Combination of Preclinical Models. Mol Cancer Res. 2022;OF1–4.

48. Shah OS, Chen F, Webn A, Kashiparekh A, Savariau L, Clifford B, et al. The invasive lobular cancer cell line encyclopedia (ICLE) for studying potential biomarkers and exploring therapeutic opportunities. 2023 [cited 2023 Oct 22];2023.09.26.559548. Available from: https://www.biorxiv.org/content/10.1101/2023.09.26.559548v1

49. Sikora MJ, Jacobsen BM, Levine K, Chen J, Davidson NE, Lee AV, et al. WNT4 mediates estrogen receptor signaling and endocrine resistance in invasive lobular carcinoma cell lines. Breast Cancer Res BCR. 2016;18:92.

50. Du T, Sikora MJ, Levine KM, Tasdemir N, Riggins RB, Wendell SG, et al. Key regulators of lipid metabolism drive endocrine resistance in invasive lobular breast cancer. Breast Cancer Res BCR. 2018;20:106.

51. Agostinetto E, Nader-Marta G, Paesmans M, Ameye L, Veys I, Buisseret L, et al. ROSALINE: a phase II, neoadjuvant study targeting ROS1 in combination with endocrine therapy in invasive lobular carcinoma of the breast. Future Oncol Lond Engl. 2022;18:2383–92.

52. Voorwerk L, Isaeva OI, Horlings HM, Balduzzi S, Chelushkin M, Bakker NAM, et al. PD-L1 blockade in combination with carboplatin as immune induction in metastatic lobular breast cancer: the GELATO trial. Nat Cancer. 2023;4:535–49.

53. McCart Reed AE, Lal S, Kutasovic JR, Wockner L, Robertson A, de Luca XM, et al. LobSig is a multigene predictor of outcome in invasive lobular carcinoma. NPJ Breast Cancer. Springer US; 2019;5:18–18.

54. Sflomos G, Battista L, Aouad P, De Martino F, Scabia V, Stravodimou A, et al. Intraductal xenografts show lobular carcinoma cells rely on their own extracellular matrix and LOXL1. EMBO Mol Med. 2021;13:e13180.

55. Olukoya AO, Stires H, Bahnassy S, Persaud S, Guerra Y, Ranjit S, et al. Riluzole Suppresses Growth and Enhances Response to Endocrine Therapy in ER+ Breast Cancer. J Endocr Soc. 2023;7:bvad117.

56. Van Baelen K, Geukens T, Maetens M, Tjan-Heijnen V, Lord CJ, Linn S, et al. Current and future diagnostic and treatment strategies for patients with invasive lobular breast cancer. Ann Oncol Off J Eur Soc Med Oncol. 2022;33:769–85.

57. Sikora MJ, Cooper KL, Bahreini A, Luthra S, Wang G, Chandran UR, et al. Invasive lobular carcinoma cell lines are characterized by unique estrogen-mediated gene expression patterns and altered tamoxifen response. Cancer Res. 2014;74:1463–74.

58. Xie Z, Bailey A, Kuleshov MV, Clarke DJB, Evangelista JE, Jenkins SL, et al. Gene Set Knowledge Discovery with Enrichr. Curr Protoc. 2021;1:e90–e90.

59. Sikora MJ, Johnson MD, Lee AV, Oesterreich S. Endocrine Response Phenotypes Are Altered by Charcoal-Stripped Serum Variability. Endocrinology. 2016;157:3760–6.

60. Cerami E, Gao J, Dogrusoz U, Gross BE, Sumer SO, Aksoy BA, et al. The cBio cancer genomics portal: an open platform for exploring multidimensional cancer genomics data. Cancer Discov. 2012;2:401–4.

61. Rao DM, Shackleford MT, Bordeaux EK, Sottnik JL, Ferguson RL, Yamamoto TM, et al. Wnt family member 4 (WNT4) and WNT3A activate cell-autonomous Wnt signaling independent of porcupine O-acyltransferase or Wnt secretion. J Biol Chem. 2019;294:19950–66.

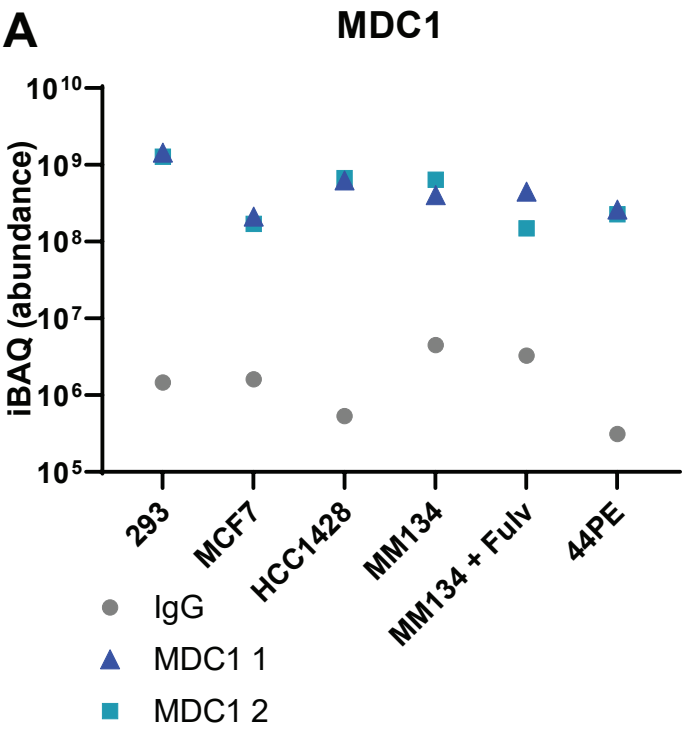

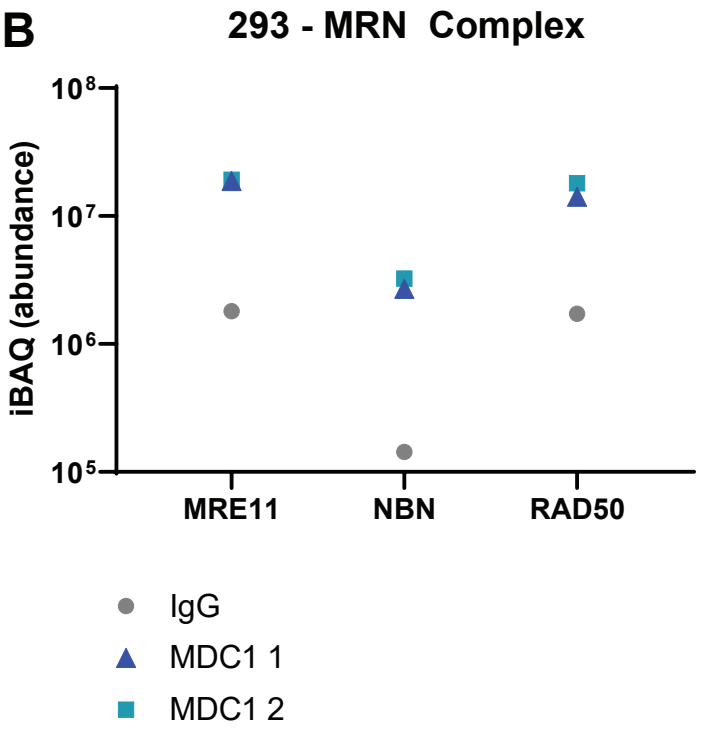

C 293 - Enriched Pathways (GO Biological Processes)

Term	Overlap	adj.p
DNA metabolic process (GO:0006259)	68/277	9.06E-20
transcription, DNA-templated (GO:0006351)	58/221	2.35E-18
DNA repair (GO:0006281)	68/298	2.46E-18
chromatin remodeling (GO:0006338)	36/103	2.18E-15
transcription elongation from RNA polymerase II promoter (GO:0006368)	29/67	3.74E-15
transcription by RNA polymerase II (GO:0006366)	65/320	5.73E-15
DNA-templated transcription, elongation (GO:0006354)	29/69	7.13E-15
cellular response to DNA damage stimulus (GO:0006974)	68/350	8.62E-15
negative regulation of cellular macromolecule biosynthetic process (GO:2000113)	88/547	3.71E-14
ATP-dependent chromatin remodeling (GO:0043044)	22/42	1.20E-13

DNA repair (GO:0006281)

MDC1
FEN1
SETD2
TRRAP
MPG
CETN2
NUCKS1
HERC2
TRIM28
NBN
KPNA2
MEN1
PIAS4
RFC5
UPF1
RFC4
PARP1
PARP2
RFC2
LIG3
WRNIP1
CSNK1E
CHD1L
ACTR8
BAZ1B
SMC1A
RAD23B
INIP
REXO4
DDB1
MSH6
MSH2
MSH3
TP53
BLM
VCP
PRKDC
DOT1L
IGHMBP2
XPC
BRCC3
PDS5A
MTA1
RAD21
POLD1
NSD2
ASCC2
ASCC3
FANCI
NPM1
XRCC5
INTS3
SMARCA5
RPA1
HMGA2
GTF2H1
GTF2H3
APTX
GTF2H4
GTF2H5
RAD50
ERCC3
RPA3
ERCC2
CDK1
TRIP13
MNAT1
NOP53

ATP-dependent chromatin remodeling (GO:0043044)

MBD3
SMARCE1
HDAC2
SMARCD2
PBRM1
SMARCC1
SMARCB1
HDAC1
CHD8
MBD2
SMARCA5
CHD4
CHD3
ACTR8
SMARCA1
ARID1B
SMARCA2
ACTB
GATAD2B
SMARCA4
SMARCAD1
MTA2

Supplemental Figure 1. MDC1 is strongly enriched in IP/MS and key DNA repair partners are identified in 293 cells. (A) iBAQ abundance values for MDC1 peptides for biological duplicate MDC1 IP and IgG controls. **(B)** iBAQ abundance values from 293 cells, for MRN complex proteins as positive control for identifying previously reported constitutive MDC1 partners in 293 cells. **(C)** Gene set enrichment against GO Biological Processes, with identified proteins in two highlighted pathways at right.

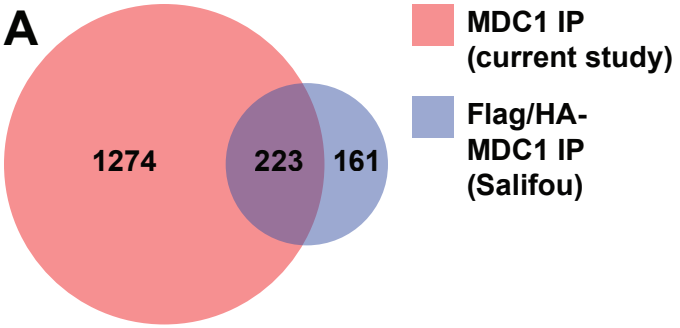

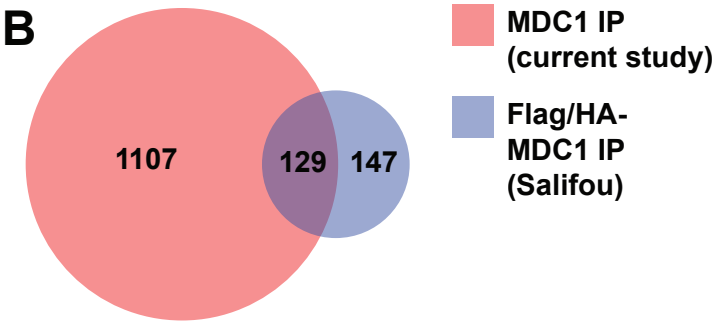

Unfiltered: GO-Biological Processes

		adj.p
MDC1 IP specific		
1	ribosome biogenesis (GO:0042254)	2.97E-58
2	ncRNA processing (GO:0034470)	3.23E-56
3	rRNA processing (GO:0006364)	2.44E-54
4	rRNA metabolic process (GO:0016072)	2.70E-50
5	gene expression (GO:0010467)	8.94E-34
6	mRNA processing (GO:0006397)	1.53E-28
Shared		
1	RNA splicing, via transesterification reactions with bulged adenosine as nucleophile (GO:0000377)	3.26E-54
2	mRNA splicing, via spliceosome (GO:0000398)	2.22E-52
3	gene expression (GO:0010467)	2.22E-52
4	mRNA processing (GO:0006397)	3.77E-50
5	nuclear-transcribed mRNA catabolic process, nonsense-mediated decay (GO:0000184)	1.08E-45
6	cytoplasmic translation (GO:0002181)	1.94E-42
Flag/HA-MDC1 IP specific		
1	mRNA splicing, via spliceosome (GO:0000398)	6.31E-13
2	RNA splicing, via transesterification […] (GO:0000377)	8.44E-12
3	mRNA processing (GO:0006397)	1.63E-10
4	anaphase-promoting complex-dependent catabolic process (GO:0031145)	4.02E-07
5	regulation of cell cycle phase transition (GO:1901987)	1.09E-06
6	proteasomal ubiquitin-independent protein catabolic process (GO:0010499)	3.12E-06

Filtered: GO-Biological Processes

		adj.p
MDC1 IP specific		
1	transcription, DNA-templated (GO:0006351)	2.45E-14
2	transcription elongation from RNA polymerase II promoter (GO:0006368)	5.43E-14
3	chromatin remodeling (GO:0006338)	5.43E-14
4	DNA metabolic process (GO:0006259)	6.87E-14
5	DNA-templated transcription, elongation (GO:0006354)	6.99E-14
6	DNA repair (GO:0006281)	7.38E-14
Shared		
1	metaphase/anaphase transition of cell cycle (GO:0044784)	4.21E-08
2	metaphase/anaphase transition of mitotic cell cycle (GO:0007091)	4.21E-08
3	positive regulation of metaphase/anaphase transition of cell cycle (GO:1902101)	2.15E-06
4	positive regulation of mitotic metaphase/anaphase transition (GO:0045842)	2.15E-06
5	positive regulation of mitotic sister chromatid separation (GO:1901970)	2.15E-06
6	regulation of cell cycle phase transition (GO:1901987)	2.44E-06
Flag/HA-MDC1 IP specific		
1	anaphase-promoting complex-dependent catabolic process (GO:0031145)	6.48E-07
2	regulation of cell cycle phase transition (GO:1901987)	1.11E-06
3	proteasomal ubiquitin-independent protein catabolic process (GO:0010499)	3.55E-06
4	gluconeogenesis (GO:0006094)	5.06E-06
5	hexose biosynthetic process (GO:0019319)	6.78E-06
6	regulation of mitotic cell cycle (GO:0007346)	1.56E-05

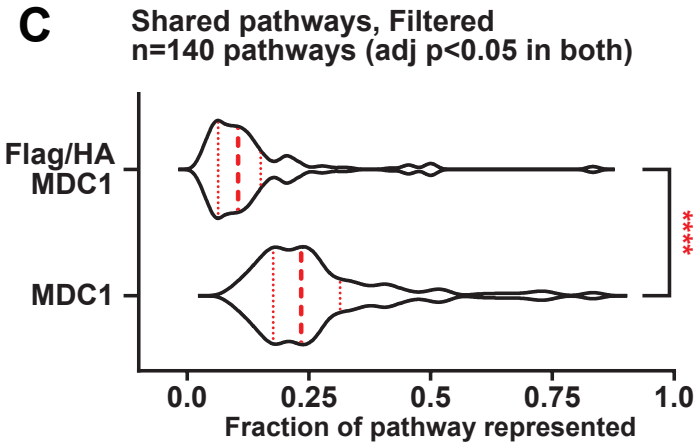

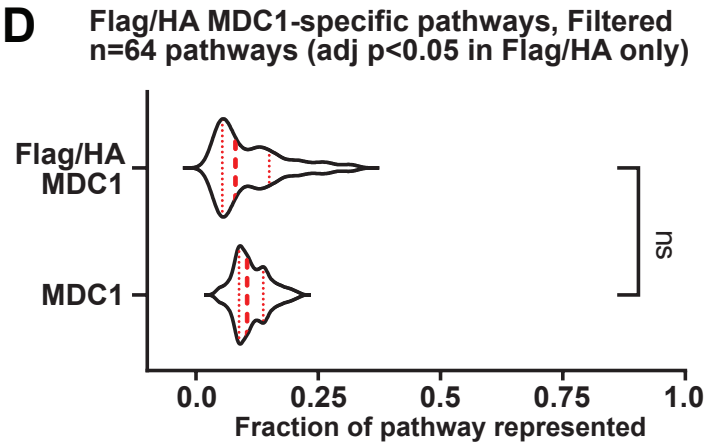

Supplemental Figure 2. MDC1 IP/MS with specific antibody provided greater depth in pathway coverage and new target compared to affinity tag IP/MS. (A-B) Comparing 293 MDC1 IP/MS versus hits reported by Salifou et al (see text). **(A)** Gene set enrichment against GO Biological Processes, without filtering hits from RNA metabolic pathways, from study-specific versus shared MS hits. **(B)** Gene set enrichment against GO Biological Processes, after filtering hits from RNA metabolic pathways. DNA repair and associated pathways were among the top hits only from MDC1 antibody IP/MS. **(C)** MDC1 IP/MS provided greater pathway coverage among GO BP pathways enriched in both IP/MS studies. ****, t-test, $p<0.0001$. **(D)** For pathways that were enriched specifically in Salifou et al affinity tag IP/MS, MDC1 IP/MS provided equivalent pathway coverage in identified peptides.

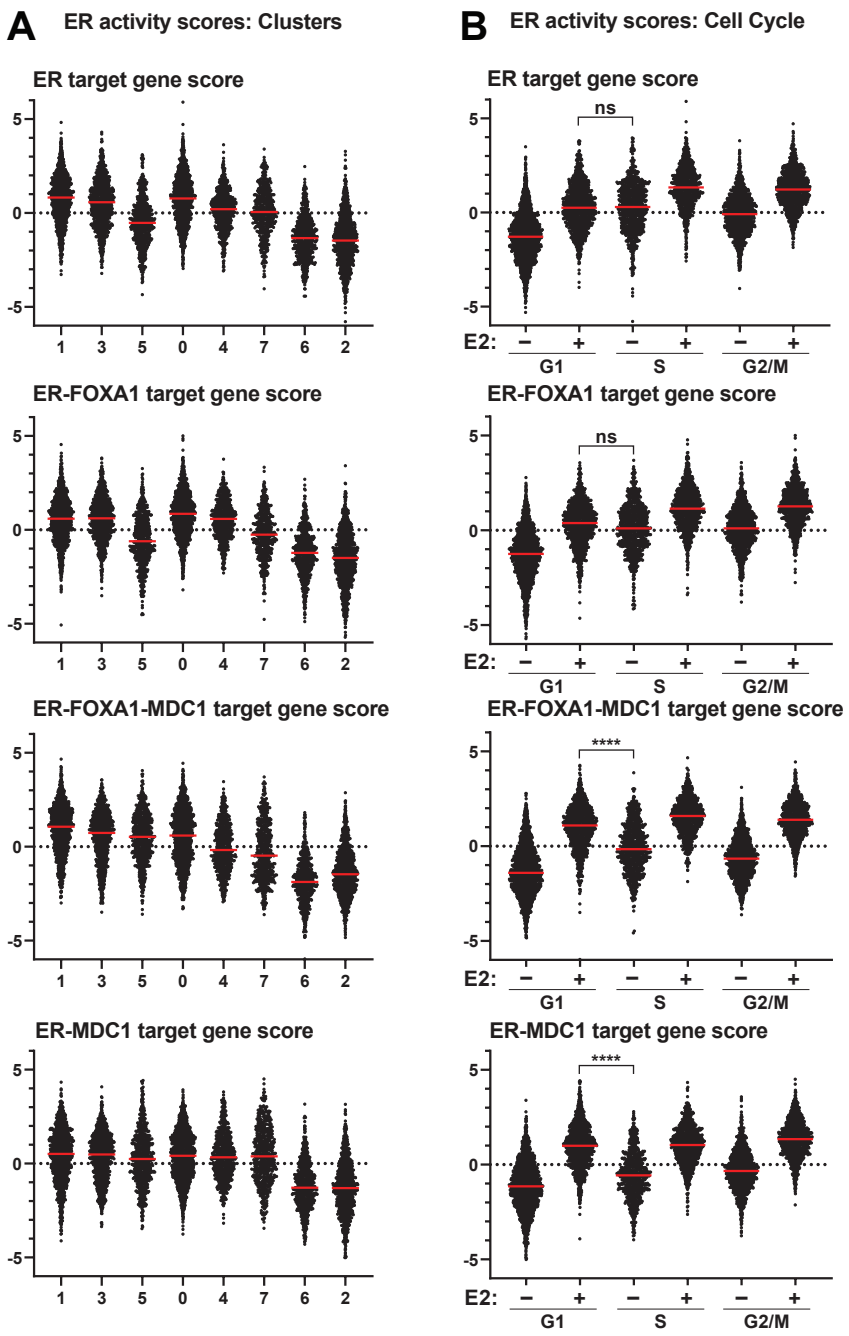
A
ER activity scores: Clusters
B
ER activity scores: Cell Cycle
ER target gene score
ER-FOXA1 target gene score
ER-FOXA1-MDC1 target gene score
ER-MDC1 target gene score
5
0
-5
1
3
5
0
4
7
6
2
ns
****
E2:
−
+
G1
S
G2/M

Supplemental Figure 3. ER target gene sets and FOXA1 vs MDC1 activity are distinct across gene expression clusters, cell cycle status, and treatment group. (A) Single cell data represented by the heatmap in Figure 3C, red line = median score, points = individual cells. **(B)** ER target gene set scores by treatment (±E2) and predicted cell cycle state. Comparison between G1/+E2 and S/–E2 is representative of the cell cycle-dependent increase in non-MDC1 target genes (ER, ER-FOXA1 targets) compared to MDC1 target genes (ER-FOXA1-MDC1, ER-MDC1); i.e. for the former, target gene scores are increased in S/G2 relative to G1 regardless of estrogen treatment. ****, ANOVA, adj.p <0.0001.

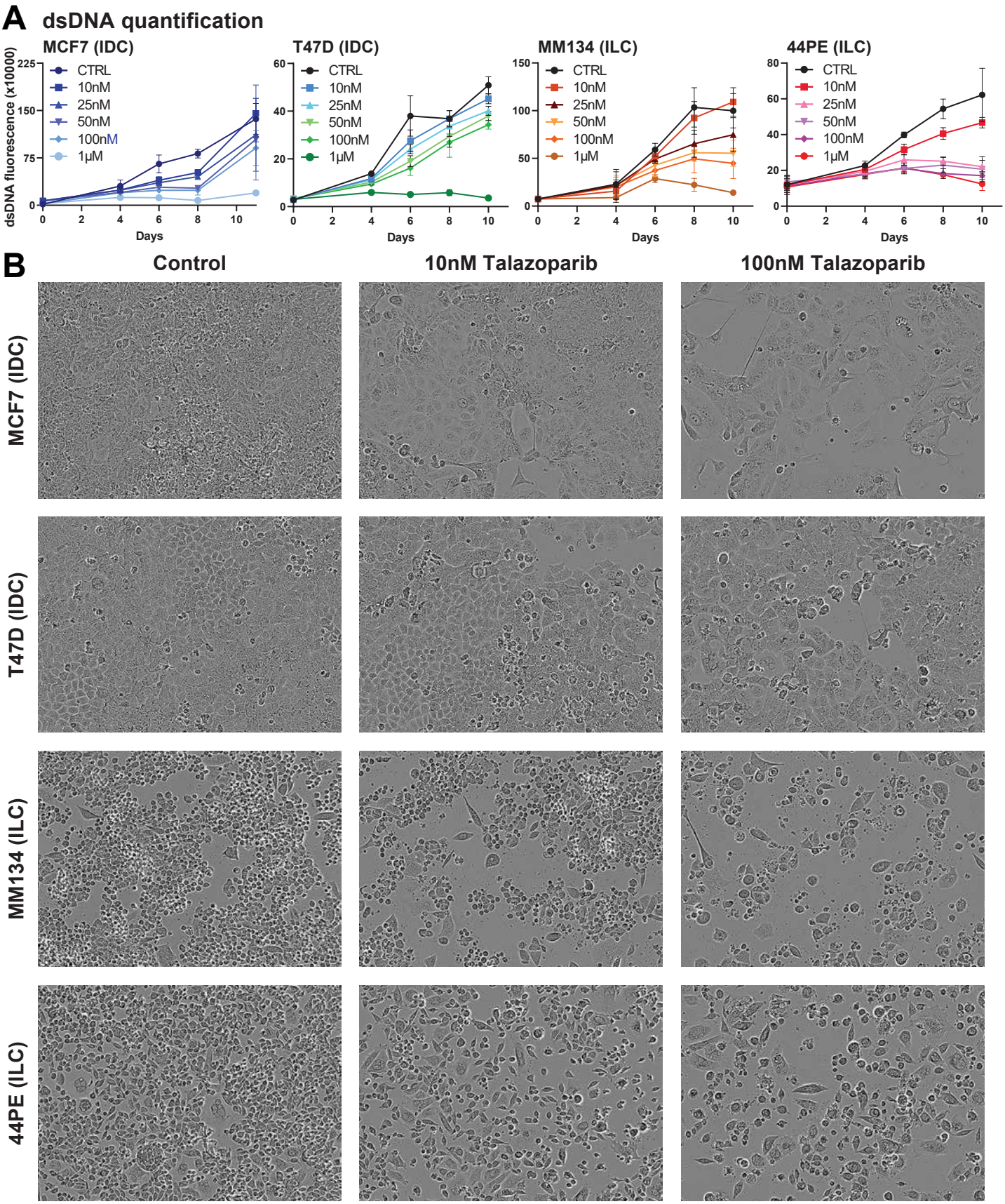
A
dsDNA quantification
MCF7 (IDC)
T47D (IDC)
MM134 (ILC)
44PE (ILC)
dsDNA fluorescence (x10000)
CTRL
10nM
25nM
50nM
100nM
1μM
Days
B
Control
10nM Talazoparib
100nM Talazoparib
MCF7 (IDC)
T47D (IDC)
MM134 (ILC)
44PE (ILC)

Supplemental Figure 4. ILC cells are sensitive to PARPi talazoparib *in vitro*. (A) Time course of cell proliferation, assessed by dsDNA quantification, with increasing concentration of talazoparib. Extended >7d suggest decreased long-term viability in ILC cells specifically after the single talazoparib treatment. **(B)** Representative Incucyte images after 9 days of treatment as indicated. Remaining IDC cells are fewer than control but morphologically appear healthy and viable, whereas ILC cells show irregular morphology consistent with apoptosis or other cell death.

A

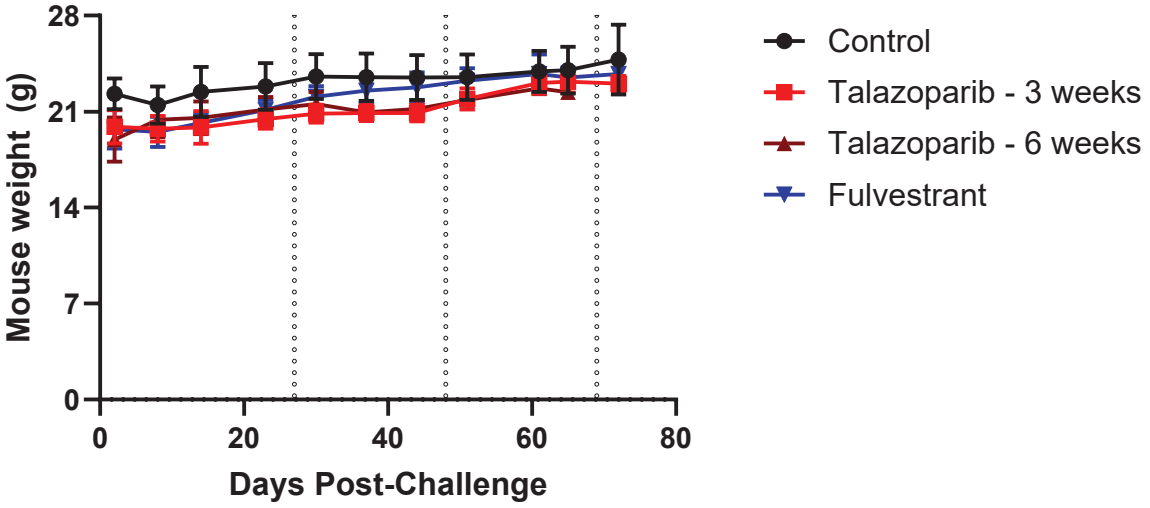
Mouse weight (g)
28
21
14
7
0
0
20
40
60
80
Days Post-Challenge
Control
Talazoparib - 3 weeks
Talazoparib - 6 weeks
Fulvestrant

B

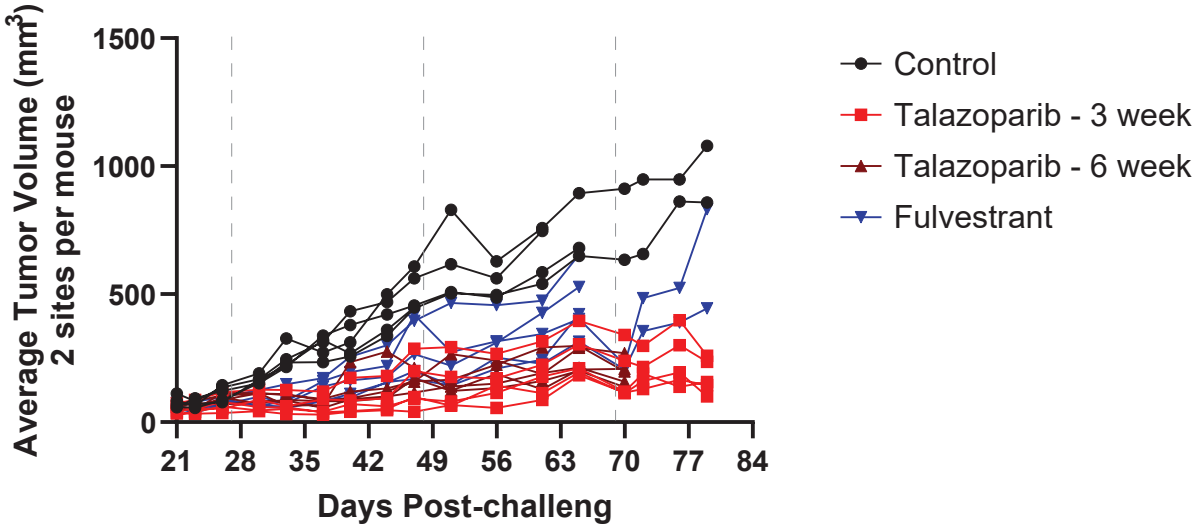
Average Tumor Volume (mm3)
2 sites per mouse
1500
1000
500
0
21
28
35
42
49
56
63
70
77
84
Days Post-challeng
Control
Talazoparib - 3 week
Talazoparib - 6 week
Fulvestrant

Supplemental Figure 5. ILC cells are sensitive to PARPi talazoparib *in vivo*. (A) Mouse weights during treatment time-course. No significant impact of treatment on weight was observed. **(B)** Data as in Figure 7A, shown as mean tumor volume per mouse (n=5 mice per arm).